

UC Davis

UC Davis Previously Published Works

Title

Impacts of model resolution and ocean coupling on mean and eddy momentum transfer during the rapid intensification of super-typhoon Muifa (2011)

Permalink

<https://escholarship.org/uc/item/4j59w07p>

Journal

Quarterly Journal of the Royal Meteorological Society, 148(749)

ISSN

0035-9009

Authors

Yu, Yang
Chen, Shu-Hua
Tseng, Yu-Heng
[et al.](#)

Publication Date

2022-10-01



DOI

10.1002/qj.4379

Peer reviewed

RESEARCH ARTICLE

Impacts of model resolution and ocean coupling on mean and eddy momentum transfer during the rapid intensification of super-typhoon *Muifa* (2011)

Yang Yu^{1,2}  | Shu-Hua Chen¹  | Yu-Heng Tseng³ | Gregory R. Foltz⁴ | Rong-Hua Zhang^{2,5} | Huiwang Gao⁶

¹Department of Land, Air, and Water Resources, University of California, Davis, California, USA

²Key Laboratory of Ocean Circulation and Waves, Institute of Oceanology and Center for Ocean Mega-Science, Chinese Academy of Sciences, Qingdao, China

³Institute of Oceanography, National Taiwan University, Taipei, Taiwan

⁴NOAA/Atlantic Oceanographic and Meteorological Laboratory, Miami, Florida, USA

⁵School of Marine Sciences, Nanjing University of Information Science and Technology, Nanjing, China

⁶Key Laboratory of Marine Environment and Ecology, Ministry of Education of China, Ocean University of China, Qingdao, China

Correspondence

S.-H. Chen, Department of Land, Air, and Water Resources, University of California, One Shields Avenue, Davis, CA 95616, USA.

Email: shachen@ucdavis.edu

Funding information

China Scholarship Council; National Oceanic and Atmospheric Administration; National Science Foundation, Grant/Award Number: 1624414-0; Special Funds of Shandong Province for Pilot National Laboratory for Marine Science and Technology (Qingdao), Grant/Award Number: 2022QNLMO10301-4; Startup Foundation for Introducing Talent of NUIST

Abstract

This study uses a coupled atmosphere–ocean model with different numerical settings to investigate the mean and eddy momentum transfer processes responsible for Typhoon *Muifa*'s (2011) early rapid intensification (RI). Three experiments are conducted. Two use the coupled model with a horizontal resolution of either 1 km (HRL) or 3 km (LRL). The third (NoTCFB) is the same as LRL but excludes tropical cyclone (TC)-induced sea-surface temperature (SST) cooling. HRL reasonably reproduces *Muifa*'s intensity during its rapid intensification and weakening periods. The azimuthal mean tangential and radial momentum budgets are analysed before the RI rates diverge between HRL and LRL. Results show that the dominant processes responsible for *Muifa*'s intensification are different in HRL and LRL. For HRL, the net eddy effect intensifies the storm's circulation and contracts the eyewall during early RI, and it dominates the net mean-flow effect inside the radius of maximum wind (RMW), except near the surface and between 2 and 5 km close to the RMW. In contrast, the mean and eddy effects in LRL almost cancel inside the RMW, while the mean-flow effects dominate and intensify tangential winds outside. Without TC-induced SST cooling, *Muifa* in NoTCFB reaches a similar storm intensity as in HRL but its rapid weakening rate is substantially underestimated. The dominant mechanisms for tangential wind intensification in NoTCFB are similar to those in LRL, but their magnitudes are larger, implying a misrepresentation of the dominant momentum transfer processes in NoTCFB during RI. For the radial momentum budget analysis, the dominant processes are similar among the three experiments except for some differences in their locations and strengths.

KEYWORDS

eddy processes, momentum budget analysis, rapid intensification, tropical cyclone

1 | INTRODUCTION

Tropical cyclones (TCs), commonly known as typhoons in the western North Pacific (WP) and hurricanes in the eastern North Pacific (EP) and North Atlantic (AL), are among the most destructive weather phenomena in the world. In the past three decades, TC track prediction has improved substantially, but improvements in TC intensity prediction have progressed more slowly (DeMaria *et al.*, 2007; 2014). TC tracks are largely controlled by the large-scale environmental steering flow (Chan, 2005). Continuous improvements in ensemble forecasts and data assimilation have enabled numerical weather prediction (NWP) systems to better represent the large-scale atmospheric flow steering TCs, resulting in improved TC track predictions (Abersson, 2001; Franklin *et al.*, 2003; Dong and Zhang, 2016; Landsea and Cangialosi, 2018). But, in addition to the influence of the large-scale environment, TCs' intensity changes, and in particular rapid intensification (RI), involve cloud-scale processes, internal dynamics, and multi-scale interactions within TCs. These are still not well understood and potentially not well-resolved by current NWP model resolutions, lowering intensity prediction skill (Trabing and Bell, 2020).

RI is defined as an increase in a TC's maximum 10 m wind speed (V_{max}) of at least 15.4 m s^{-1} (~ 30 knots) in 24 hr (Kaplan and DeMaria, 2003) or a decrease in the storm's minimum sea-level pressure (MSLP) of at least 42 hPa in 24 hr (Holliday and Thompson, 1979). RI occurs at least once during most intense TCs' lifetimes. On average, 37% of WP TCs (Wang and Zhou, 2008), 42% of EP TCs (Wang and Jiang, 2021), and 31% of AL TCs (Kaplan and DeMaria, 2003) undergo RI. Though all category-4 and -5 hurricanes on the Saffir–Simpson hurricane scale (SSH: Simpson and Saffir, 1974) and 90% of super-typhoons (category-5 typhoons on SSH) undergo RI at least once (Wang and Zhou, 2008), RI remains challenging to predict. For example, small environmental perturbations may change a TC's structure during RI and result in large intensity changes (Zhang and Tao, 2013; Judt and Chen, 2016; Li *et al.*, 2019).

Many studies have investigated the mechanisms that lead to RI, including the environmental conditions (Kaplan and DeMaria, 2003; Kaplan *et al.*, 2015) and TC multi-scale interactions (Judt *et al.*, 2016; Judt and Chen, 2016). For the large-scale environment, for example, the impacts of sea-surface temperature (SST) and vertical wind shear on RI have been widely studied (Hendricks *et al.*, 2010; Črnivec *et al.*, 2016; Fudeyasu *et al.*, 2018; Chih and Wu, 2020). SST influences the amount of energy available for TC development through latent and sensible heat fluxes (Malkus and Riehl, 1960) and determines the maximum potential intensity that a TC can

achieve (Demaria and Kaplan, 1994; Emanuel, 1999; Zeng *et al.*, 2007; Foltz *et al.*, 2018). Vertical wind shear influences TCs through its impact on vertical alignment of the vortex in the lower and middle levels and convective activity, as well as dry air intrusion and precipitation, which provide feedbacks to TC intensity (Zhang and Tao, 2013; Nguyen and Molinari, 2015; Tao and Jiang, 2015; Tao and Zhang, 2015). Besides the environmental influence, a TC's internal dynamics may govern whether the storm undergoes RI. RI is usually associated with intense inner-core (eyewall) convective bursts (Steranka *et al.*, 1986; Sanger *et al.*, 2014) and asymmetric convective structures (Zhang *et al.*, 2001; Montgomery *et al.*, 2006; Van Sang *et al.*, 2008; Fang and Zhang, 2011; Persing *et al.*, 2013; Kilroy and Smith, 2016). The asymmetric eddy processes can change a TC's intensity through the barotropic and baroclinic energy cascade (Bhalachandran *et al.*, 2020). A gradient wind forcing in the friction layer contributes to the spin-up of RI (Montgomery *et al.*, 2020).

As computational resources have significantly increased, state-of-the-art NWP systems have increasingly used cloud-resolving resolutions (usually higher than 5 km) to capture TC internal dynamics (Judt *et al.*, 2016; Li *et al.*, 2019). Some studies have shown that high-resolution cloud-permitting NWP models have improved representations of TC structures such as spiral rain bands and secondary circulations (Rogers, 2010; Gopalakrishnan *et al.*, 2011; 2012; Jin *et al.*, 2014). However, most of these studies utilized atmospheric models alone. Increasing model resolution in an NWP system that only has an atmospheric component can better capture a storm's intensity but may cause other problems. For example, the Taiwan Central Weather Bureau recently improved its Typhoon Weather Research and Forecast (TWRf) model by increasing its spatial resolution from 15 to 3 km. The cloud-resolving (3 km) TWRf model can better predict RI and has lowered the intensity forecast errors for lead times of 0–48 hr. However, the model overestimates TC intensity when the forecast lead time is greater than 48 hr, particularly for slow-moving TCs (Leroux *et al.*, 2018; Hsiao *et al.*, 2020). This is due in part to the absence of TC–ocean interaction in the TWRf model.

TCs often have limited impacts on SST cooling before they intensify (Lin *et al.*, 2008; 2009; Sandery *et al.*, 2010; Dare and McBride, 2011). However, once a storm intensifies, TC-induced SST cooling cannot be ignored because it decreases surface latent and sensible heat fluxes, providing a negative feedback to TC intensification (Schade and Emanuel, 1999; Chan *et al.*, 2001; Sandery *et al.*, 2010; Vincent *et al.*, 2012). Despite progress, challenges remain on how SST feedback affects RI in a high-resolution atmosphere–ocean coupled system (Kanada *et al.*, 2017; Li *et al.*, 2019). While an atmosphere–ocean coupled

model may reduce atmospheric models' overestimates of storms' maximum intensities (Leroux *et al.*, 2018; Hsiao *et al.*, 2020), it can produce weaker TCs during the earlier stage of a forecast (e.g. forecast length < 48 hr), which reduces RI predictability. Thus an intuitive question to ask is "Is the commonly accepted 3 or 4 km cloud-resolving resolution capable of forecasting RI when the TC-induced SST cooling feedback is considered?" If not, what are the deficiencies compared to a model with even finer resolution, such as 1 km or higher?

In an idealized study, Montgomery *et al.* (2020) conducted a TC simulation with a 1 km resolution and applied a momentum budget analysis to investigate the contribution of mean and eddy momentum transfer during RI. One important finding in their study is that the asymmetric (eddy) wind component and unbalanced mean gradient wind flow contribute substantially to TC intensification within the radius of maximum wind (RMW). Our study is different from that of Montgomery *et al.* (2020) in that it explores how mean and eddy momentum transfer during RI may change under different model resolutions and TC-induced SST feedback, using super-typhoon *Muifa* (2011) as a case-study. More specifically, we use an atmosphere–ocean coupled model for numerical simulations, while Montgomery *et al.* used an atmospheric model alone. In addition, ours is a real case-study with the use of a sophisticated microphysics scheme, while theirs was an idealized case-study using a simple warm microphysics scheme. They also excluded radiation parametrization in their simulation. However, our momentum budget analysis mainly follows Montgomery *et al.* (2020).

This article is organized as follows. Section 2 introduces the model and numerical experiments used in this study. Section 3 presents model results and the dominant processes responsible for early RI changes when applying different atmospheric resolutions and TC–ocean coupling feedback. Summary and conclusions are provided in Section 4.

2 | NUMERICAL MODEL AND EXPERIMENT DESIGN

2.1 | Super-typhoon *Muifa* (2011)

Typhoon *Muifa* (2011) was the ninth named TC and the second super-typhoon in the 2011 WP typhoon season. *Muifa* became a tropical depression on 27 July and a named tropical storm on 28 July. At 0000 UTC 30 July, *Muifa* intensified into a category-3 typhoon on SSHS and underwent RI during 0000 to 1800 UTC 30 July. *Muifa* slowly drifted northward during its RI. Based on the China Meteorological Agency (CMA) best-track data (Ying

et al., 2014), the storm strengthened into a category-5 super-typhoon in <24 hr, reaching its peak intensity with a Vmax of 65 m s⁻¹ and MSLP of 915 hPa at 1800 UTC 30 July. *Muifa* went through rapid weakening (RW) after RI and became a category-4 typhoon on 31 July. After RW, the storm continued to move northward with relatively steady intensity and then entered the East China Sea on 6 August.

Our period of interest for this study is *Muifa*'s RI phase, while the RW period will be the focus of a follow-up study. Typhoon *Muifa* is chosen for the study because the storm underwent both RI and RW over the open ocean in the western North Pacific, making it an ideal candidate for exploring the impact of TC–ocean coupling on its intensity.

2.2 | Model description

A high-resolution atmosphere–ocean model is used to conduct numerical experiments. The coupled model used in this study is based on the Coupled Ocean–Atmosphere–Wave–Sediment Transport (COAWST) model (Warner *et al.*, 2010). The COAWST version 3.6 model consists of several components including the non-hydrostatic Weather Research and Forecasting (WRF) model (version 4.1.2: Skamarock *et al.*, 2019) for the atmosphere, the hydrostatic Regional Ocean Modeling System (ROMS) model (version 3.9: Shchepetkin and McWilliams, 2005) for the ocean, and the Simulating Waves Nearshore model (version 41.31: Booij *et al.*, 1999) for surface waves. All model components have been successfully used in a broad range of applications. In this study, we use only the WRF and ROMS (WRF-ROMS) components in order to include ocean–atmosphere coupled feedback in *Muifa*'s intensity prediction.

2.3 | Numerical setting

Figure 1 shows the domains of WRF (black boxes) and ROMS (the red box) that are used in this study. WRF uses four nested domains with horizontal resolutions of 27, 9, 3 and 1 km and domain sizes of 280 × 280, 541 × 541, 403 × 403 and 802 × 802 grid points, respectively, referred to as d01 to d04. The outer two WRF domains (d01 and d02) are fixed in location, while the inner two domains (d03 and d04) are moving nests that follow the TC centre, defined by the minimum geopotential height at 850 hPa. In the vertical direction, the WRF model has 45 levels in a stretched grid, with a higher resolution near the surface. The model top is at 50 hPa. The WRF parametrizations include the unified Noah land surface model (Tewari *et al.*, 2004), the revised fifth-generation Mesoscale Model (MM5) Monin–Obukhov surface layer scheme (Jiménez

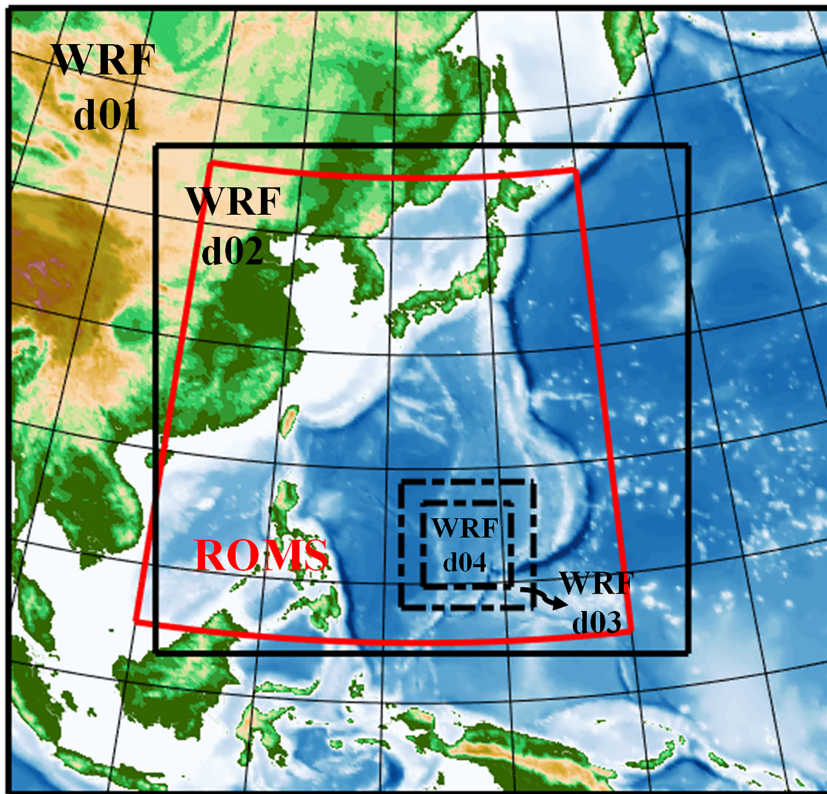


FIGURE 1 Model domain and topography. Black boxes are WRF domains with horizontal resolutions of 27, 9, 3 and 1 km for d01 to d04, respectively. The red box is the ROMS domain with a horizontal resolution of 9 km. WRF domains d03 and d04 are moving nests that automatically move following the storm centre, defined by the minimum 850 hPa geopotential height over the tropical cyclone region [Colour figure can be viewed at wileyonlinelibrary.com]

et al., 2012), the Shin–Hong scale-aware planetary boundary layer (PBL) scheme (Shin and Hong, 2015), the Rapid Radiative Transfer Model for General circulation models (RRTMG) for short-wave and long-wave radiation (Iacono *et al.*, 2008), and the Purdue Lin microphysics scheme for resolved cloud processes (Chen and Sun, 2002). The Kain–Fritsch (KF) cumulus scheme (Kain, 2004) is applied to d01 and d02 only. Both the initial and lateral boundary conditions of the WRF model are extracted from the National Centers for Environmental Prediction (NCEP) Global Forecast System (GFS) Final Analysis (FNL) with a horizontal resolution of 1° (~ 108 km) and a temporal resolution of 6 hr. As SST feedback is important for our study and SST varies significantly in space, differences in the experiments' forecasted TC tracks can influence the results and potentially bias our conclusions. Thus, to improve TC track simulations, meteorological conditions (e.g. winds, temperature and moisture) above the PBL in d01 and d02 are nudged to FNL data using different nudging techniques. Four-dimensional grid nudging (FDDA: Stauffer and Seaman, 1994; Liu *et al.*, 2008) is applied to d01 to ease the transition from FNL global model data to WRF model simulations. This is necessary due to the use of different physics parametrizations and numerical methods in these two models. Spectral nudging (Miguez-Macho *et al.*, 2004) with wavelengths greater than 700 km is applied to d02. This is to ensure that the large-scale steering flow is well-simulated and produces a

realistic TC track while still allowing smaller-scale features to develop in d02 and propagate into d03 through boundary conditions, aiding the development of TC intensity in d03. There is no nudging employed in d03 and d04 so that the TC can freely develop in those domains.

In this study, the ROMS model uses a single fixed domain (red box in Figure 1) with a horizontal resolution of $1/12^\circ$ (~ 9 km) covering 110° to 150° E and 5° to 45° N. The ROMS model has 40 layers in the vertical direction, with higher resolutions near the sea surface generated from Shchepetkin's double stretching function (Shchepetkin and McWilliams, 2009). The ROMS parametrizations are the same as those used in Yu *et al.* (2017; 2020), including Mellor–Yamada level-2.5 scheme (Mellor and Yamada, 1982) for vertical mixing and Smagorinsky scheme (Smagorinsky, 1963) for horizontal diffusion. Short-wave radiation penetration in the ocean is modelled using a double exponential irradiance absorption function (Paulson and Simpson, 1977) with Jerlov water type I parameters over the open ocean (deeper than 200 m) and Jerlov water type II parameters in the marginal seas (water depth shallower than 200 m). The wind stress and latent and sensible heat fluxes are calculated using the COARE 3.0 bulk formula (Fairall *et al.*, 1996b; 2003) with an effective wind speed correction method (Bye and Wolff, 1999). Note that the wind stress accounts for a levelling off of the drag coefficient for winds greater than $30\text{--}40$ m s $^{-1}$ (Powell *et al.*, 2003). The “cool skin” effect on surface heat fluxes

TABLE 1 List of model experiments conducted in this study

Experiments	Description
HRL	Use the WRF-ROMS coupled model with four WRF domains (the highest resolution 1 km)
LRL	Same as HRL but only three WRF domains (the highest resolution 3 km)
NoTCFB	Use the WRF model only with three domains (the highest resolution 3 km). SST is provided by another WRF-ROMS coupled simulation with the TC vortex removed in the initial conditions, which removes SST cooling induced by <i>Muifa</i> .

is also included in the model using an empirical correction scheme (Fairall *et al.*, 1996a). The lateral boundary conditions of the ROMS model are derived from the daily frequency 1/12° (~9 km) resolution HYbrid Coordinate Ocean Model (HYCOM) Global Ocean Forecasting System (GOFS) 3.1 reanalysis. The initial conditions of the ROMS model are obtained from a spin-up run, which is an ROMS-alone simulation, initialized with the HYCOM data on 1 July 2011 and forced with HYCOM and NCEP National Center for Atmospheric Research (NCEP/NCAR) reanalysis as its lateral boundary conditions and atmospheric forcing, respectively. Harmonic constants of 10 principal tidal constituents (M2, S2, N2, K2, K1, O1, P1, Q1, Mf and Mm) derived from the global inverse tidal model of TPXO7.0 (Egbert *et al.*, 1995; Egbert and Erofeeva, 2002) are specified at the lateral boundaries of the ROMS model as the tidal forcing.

WRF and ROMS communicate with each other every 15 min using Model Coupling Toolkit (MCT: Jacob *et al.*, 2005; Larson *et al.*, 2005; Warner *et al.*, 2008). WRF provides sea-level pressure, 10 m wind, 2 m temperature, 2 m relative humidity, surface long-wave and short-wave radiation fluxes, and surface evaporation and precipitation rates to ROMS, which in turn provides SST to WRF. The interpolation weights between the different WRF and ROMS grids are generated by the Spherical Coordinate Remapping Interpolation Package (SCRIP: Jones, 1999).

2.4 | Experimental design

To examine the impact of model resolution on *Muifa*'s RI prediction, two numerical experiments with different atmospheric resolutions are conducted (Table 1). The first experiment, our control run with a higher model resolution (HRL), uses the WRF-ROMS coupled model with the numerical setting described in Section 2.2. This run includes four WRF domains (d01-04), with the highest resolution of 1 km in d04, and one ROMS domain (Figure 1). The second experiment (LRL) is the same as the HRL run, except that only three domains (d01-03) are used in the WRF model, with the highest resolution of 3 km in d03. In addition to these two WRF-ROMS simulations, we also carry out a numerical experiment, called NoTCFB

(Table 1), to explore the importance of TC-induced SST cooling for *Muifa*'s RI and RW prediction. NoTCFB uses the WRF model only. The WRF setting is the same as that in LRL, and SST is updated every 15 min using prescribed values. The prescribed SSTs in NoTCFB are produced by another WRF-ROMS coupled simulation, which uses the same numerical setting as in LRL except *Muifa*'s vortex in the initial conditions was removed by applying a TC vortex removal scheme (Davis and Low-Nam, 2001). Thus there is no TC-induced SST cooling in the lower boundary condition. In all experiments, the model (either WRF-ROMS or WRF alone) is integrated for 9 days from 0000 UTC 28 July to 0000 UTC 6 August 2011, and WRF data are saved every 15 min for analysis.

3 | MODEL RESULTS AND DISCUSSION

3.1 | Model results against observations

3.1.1 | TC intensity prediction

As mentioned earlier, SST differences caused by different TC track forecasts can have a great impact on TC development. Therefore, FDDA and spectral nudging were applied to WRF d01 and d02, respectively, to ensure reasonable and comparable track simulations in the experiments. As shown in Figure 2a, all experiments closely reproduce *Muifa*'s observed track, except during the early simulations when the storm's centre is difficult to identify due to its weak intensity. These well-simulated *Muifa* tracks are obtained because the use of nudging ensures that the model's flow field effectively resembles the FNL large-scale flow, which constrains *Muifa*'s movement. These reasonable TC track simulations allow us to more precisely investigate the impacts of model resolution and TC-induced SST cooling on *Muifa*'s RI and RW forecasts.

Figure 2b,c show intensity predictions in terms of Vmax and MSLP. The simulated RI in all experiments is delayed about 12 hr compared to the CMA best-track data (i.e. from 0000 UTC to 1800 UTC 30 July in observations and 1200 UTC 30 July to 1200 UTC 31 July in the model). The delay in the predicted TC's intensification

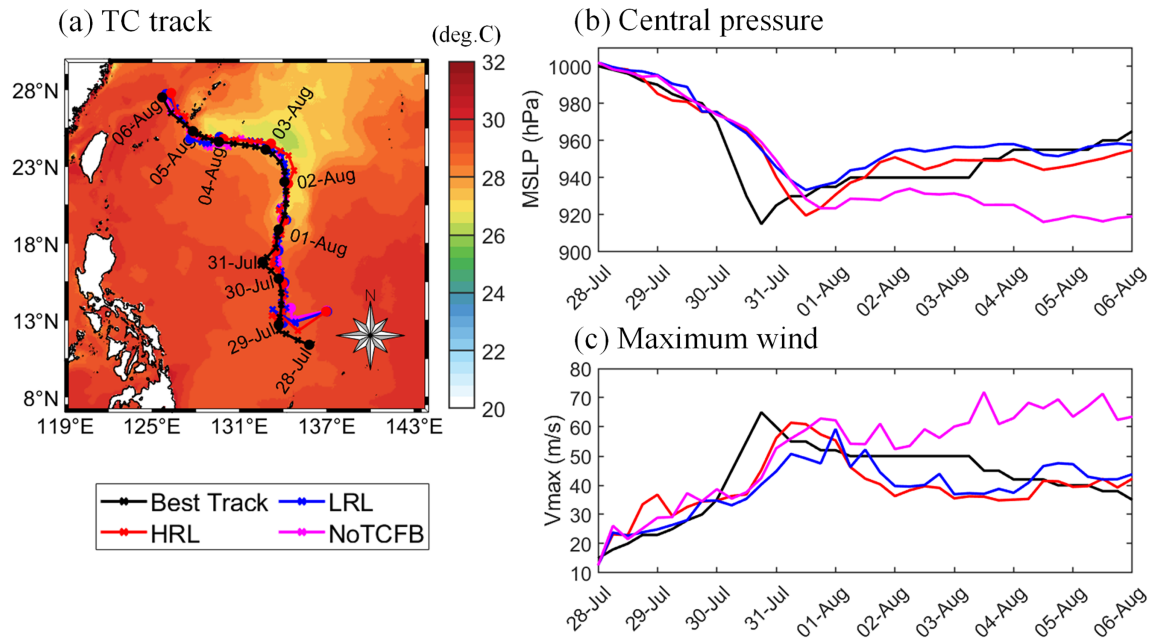


FIGURE 2 *Muifa's* track and intensity from the CMA best track (black), HRL (red), LRL (blue) and NoTCFB (purple). (a) TC track: the 6-hourly storm track (solid lines in different colours) and simulated SST in HRL (shading colour) averaged over 0000 UTC 28 July to 0000 UTC 6 August, (b) Central pressure: the storm's 6-hourly minimum sea-level pressure (MSLP), and (c) Maximum wind: the storm's 6-hourly maximum 10 m wind speed (V_{\max} , m s^{-1}) [Colour figure can be viewed at wileyonlinelibrary.com]

is not unusual. In addition to model errors (e.g. physics parametrizations), one of the reasons is related to issues with the TC's initial conditions (Chang *et al.*, 2020). An example is the incorrect position of the initial storm, which can be seen in Figure 2a, where the FNL TC location is a few hundred kilometres away from the CMA best-track location. Another possible reason is the model spin-up problem, since cloud-scale features are not present in the initial conditions. Despite the delayed start of RI in the model, the HRL experiment is able to reproduce *Muifa's* observed maximum intensity after completion of RI, though overall the model has a slightly weaker intensification rate. The HRL storm reaches a minimum MSLP of 920 hPa (Figure 2b) and highest V_{\max} of 61 m s^{-1} (Figure 2c) at 1200 UTC 31 July, compared to the observed 915 hPa and 65 m s^{-1} . With a lower resolution in LRL, the storm's maximum intensity is 935 hPa in MSLP (blue line in Figure 2b) and 50 m s^{-1} in V_{\max} (blue line in Figure 2c). LRL underestimates *Muifa's* maximum intensity by 15 hPa and 11 m s^{-1} , suggesting that in the coupled WRF-ROMS, the commonly accepted cloud-resolving resolution of 3 km cannot reproduce the observed RI and the maximum storm intensity. However, when the TC–ocean coupled feedback is turned off (i.e. NoTCFB), the WRF model with a 3 km resolution is capable of simulating *Muifa's* RI, though it greatly underestimates the RW rate after RI (magenta lines in Figure 2b,c). This result is consistent with that found in the TWRF forecast (discussed in

the Introduction), which also uses the WRF model alone with a 3 km resolution. While a high spatial resolution (e.g. 1 km) is required for the WRF model to capture convective-scale mechanisms that are important for the storm's RI, the TC-induced SST cooling feedback is critical for the TC's weakening after RI, emphasizing the importance of TC–ocean coupling in TC intensity prediction.

3.1.2 | Storm morphology during RI

We further evaluate the model forecast by comparing the simulated TC's cloud-top temperature (CTT) with observations from Multifunctional Transport Satellites series 2 (MTSAT-2; also known as Himawari 7). MTSAT-2 is a geostationary satellite that was launched in February 2006 and was operated by the Japan Meteorological Agency (JMA) until it was decommissioned in July 2015. MTSAT-2 provided imagery in five wavelength bands including one visible channel with a resolution of 1 km and four infrared channels with a resolution of 4 km. In this study the MTSAT-2 brightness temperature (BT) in the $10.3\text{--}11.3 \mu\text{m}$ infrared channel (IR1) is used.

The 6-hourly snapshots of observed IR1 BT by MTSAT-2 and simulated CTT in both HRL and LRL during 0000 UTC 30 July to 0000 UTC 31 July are shown in Figure 3. Compared to the MTSAT-2 observations (Figure 3a,d,g,j,m), HRL (Figure 3b,e,h,k,n) reasonably

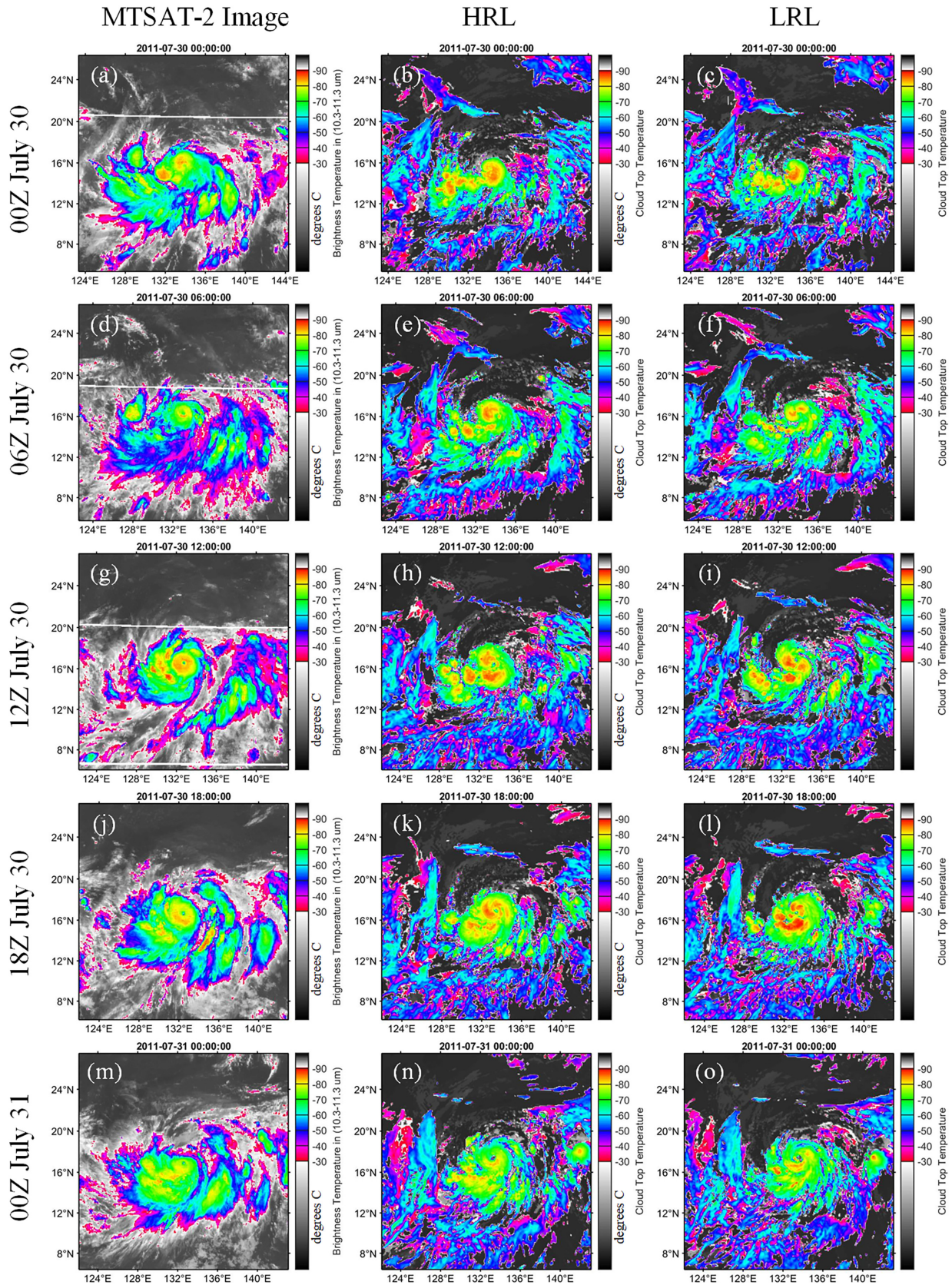


FIGURE 3 Snapshots of (a,d,g,j,m) MTSAT-2 infrared (IR) brightness temperature in the 10.3–11.3 μm band, and simulated cloud-top temperature in (b,e,h,k,n) HRL and (c,f,i,l,o) LRL at 0000 UTC, 0600 UTC, 1200 UTC and 1800 UTC 30 July and 0000 UTC 31 July 2011 [Colour figure can be viewed at wileyonlinelibrary.com]

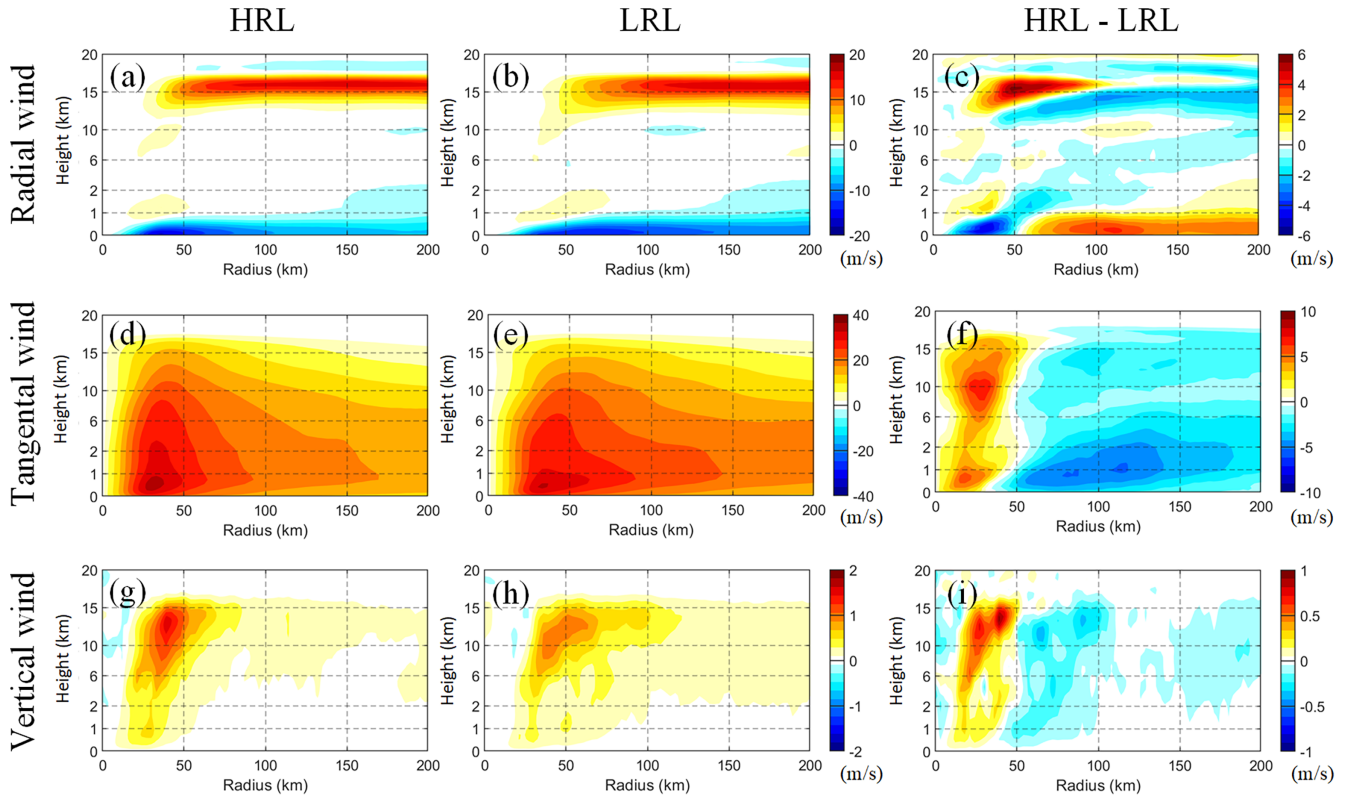


FIGURE 4 Twelve-hour averaged (a,b) radial wind, (d,e) tangential wind, (g,h) vertical wind, with respect to model storm centre from 0600 UTC to 1800 UTC 30 July 2011 in HRL and LRL, and (c,f,i) wind field differences between HRL and LRL. Note that the vertical coordinate below 2 km is expanded for better visualization [Colour figure can be viewed at wileyonlinelibrary.com]

reproduces *Muifa's* morphology during RI, including the eyewall (12 hr shift in time due to the delay of model RI) and rain bands. Although the simulated TC CTTs in HRL and LRL are similar, there are important differences. For example, at 1200 UTC 30 July, deep convective storms are embedded within an organized eyewall and the surrounding region. This is more accurately simulated in HRL than in LRL (i.e. the cyan colour region near the storm centre), when compared to observations at 0000 UTC 30 July (12 hr shift). HRL better reproduces *Muifa's* eyewall changes during RI, especially its closed cloud structure at 1800 UTC 30 July (Figure 3k versus 3L), when the storm intensities between these two experiments start diverging. At 0000 UTC 31 July, although eyewall features look similar between HRL and LRL, *Muifa's* eye is more concentrated in HRL, which is closer to observations.

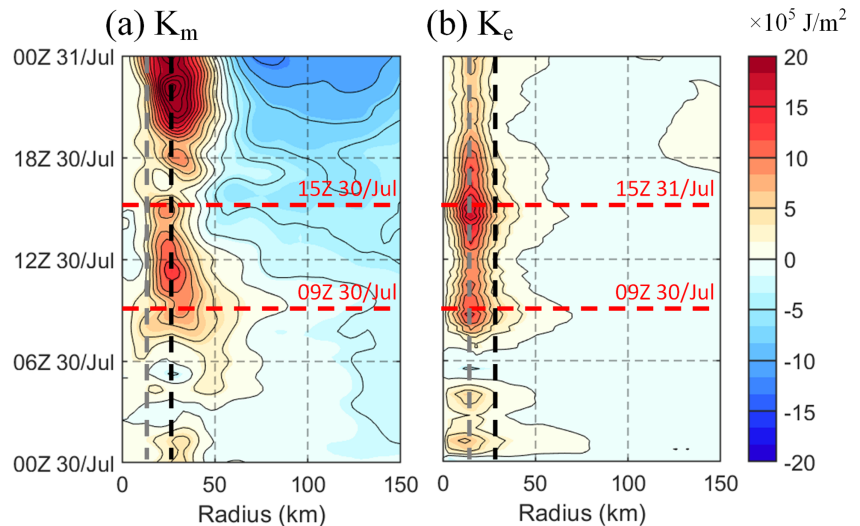
3.2 | Wind and kinetic energy analysis

Wind circulation is an important indicator of TC development. In this subsection, the azimuthally averaged wind circulation with respect to the storm centre axis is examined. The simulated TC centre locations are estimated using the pressure centroid method described in Nguyen

et al. (2014). However, instead of using the pressure field at a 2 km height as in Nguyen *et al.* (2014), we use the sea-level pressure (SLP) with a radius of 100 km and the first-guess location at the minimum SLP to estimate the TC's centroid location at each model output time (every 15 min). SLP is chosen since it is a direct model output field.

All azimuthally averaged data are from domain 3 (3 km resolution) and time-averaged data are from 15 min WRF output. Figure 4 presents the radius–height cross-sections of the storm's mean tangential, radial and vertical winds from HRL and LRL. The data are averaged from 0600 UTC to 1800 UTC 30 July during the time before the storm intensity diverges between the simulations (Figure 2b,c). Overall, the mean wind patterns from HRL and LRL are similar, as expected. Both experiments have strong inward radial winds, with maxima greater than 10 m s^{-1} within the boundary layer, and strong outward radial winds with maxima greater than 15 m s^{-1} at a height of about 16 km (Figure 4a,b). The maximum tangential wind greater than 35 m s^{-1} appears at the top of the boundary layer and is about 30–40 km away from the storm's centre (Figure 4d,e). The simulated eyewalls in HRL and LRL, identified by the strongest vertical motion, are located within a 20–50 km radius of the storm's centre

FIGURE 5 Radius–time Hovmüller diagram of column-integrated kinetic energy differences between HRL and LRL (HRL – LRL) for the azimuthally (a) symmetric and (b) asymmetric part [Colour figure can be viewed at wileyonlinelibrary.com]



axis and slope outward with height, with the maximum time-averaged vertical velocity of $\sim 1\text{--}1.5\text{ m s}^{-1}$ between 10 and 15 km height (Figure 4g,h). While their patterns are similar, there are differences between the two experiments. HRL produces stronger wind circulation, consistent with a more intense storm, as shown in Figure 2a,b. The dipole patterns in wind difference between these two experiments (Figure 4c,f,i) are mainly due to stronger winds within (outside) the eyewall in HRL (LRL), particularly the tangential component. Upward ($\sim 1\text{ km}$) and inward ($\sim 5\text{--}10\text{ km}$) shifts of the convective core (and less sloped) can also be seen in HRL. Compared to LRL, the maximum mean vertical velocity in the eyewall region in HRL is about 0.4 m s^{-1} stronger (Figure 4g versus 4h). The difference in mean tangential wind induces a stronger vertical component of relative vorticity inside the RMW for HRL but outside for LRL (figure not shown). The discussion above indicates that the application of the more expensive 1 km resolution in HRL makes the simulated eyewall circulation and convection not only stronger but also more concentrated (i.e. a smaller RMW) compared to LRL, consistent with other studies (Montgomery *et al.*, 2020).

We further calculate the azimuthally averaged symmetric (mean; K_m) and asymmetric (eddy; K_e) kinetic energy for HRL and LRL. Their differences are presented in Hovmüller diagrams. Consistent with the dipole-pattern of wind differences between the two experiments, before 1800 UTC 30 July HRL has 10 J m^{-2} higher K_m within a 50 km radius and 5 J m^{-2} lower K_m outside (Figure 5a). For the eddy kinetic energy, HRL also has a higher K_e (10 J m^{-2} more) in *Muifa's* inner core compared to LRL, but their difference is almost zero outside (Figure 5b). Moreover, the positive K_e difference is located within the radius of maximum positive K_m differences (black dashed lines in Figure 5). The time-series results show that the

difference in eddy kinetic energy between HRL and LRL in the inner core region during the earlier RI period might play an important role in the RI rate separation between the two experiments at 1800 UTC 30 July. This possibility is examined next.

3.3 | Momentum budget analysis

3.3.1 | Azimuthal mean momentum budget equations

We conduct a momentum budget analysis following Montgomery *et al.* (2020) to examine the dominant processes contributing to RI. The tangential and radial momentum equations defined in cylindrical coordinates with respect to the TC centre axis can be written, respectively, as follows:

$$\frac{\partial v}{\partial t} + u \frac{\partial v}{\partial r} + \frac{v}{r} \frac{\partial v}{\partial \lambda} + w \frac{\partial v}{\partial z} + \frac{vu}{r} + fu = -\frac{1}{\rho r} \frac{\partial p}{\partial \lambda} + F_\lambda, \quad (1)$$

$$\frac{\partial u}{\partial t} + u \frac{\partial u}{\partial r} + \frac{v}{r} \frac{\partial u}{\partial \lambda} + w \frac{\partial u}{\partial z} - \frac{v^2}{r} - fv = -\frac{1}{\rho} \frac{\partial p}{\partial r} + F_r, \quad (2)$$

where u , v and w are, respectively, the TC's radial, tangential and vertical wind components; (r, λ, z) is the coordinate vector with r the radius, λ the azimuthal angle, and z the height; f is the Coriolis parameter; ρ is the density; and p is the pressure. F_λ and F_r are the radial and tangential momentum changes induced by the sub-grid eddy-momentum flux divergence. In the WRF model simulations, these are the radial and tangential wind changes due to three-dimensional subgrid-scale diffusion and the Shin–Hong PBL parametrization. Following Montgomery *et al.* (2020), the azimuthally averaged pressure gradient term that involves the density perturbations in the

azimuthal direction is neglected due to its much smaller magnitude compared to others (Persing *et al.*, 2013). Then the budget equations for the azimuthally averaged tangential (i.e. Equation (1)) and radial momentum (i.e. Equation (2)) can be written as:

$$\underbrace{\frac{\partial \bar{v}}{\partial t}}_{V_t} = \underbrace{-\bar{u}(\bar{\zeta} + f)}_{V_{mzeta}} - \underbrace{\bar{w} \frac{\partial \bar{v}}{\partial z}}_{V_{mv}} - \underbrace{\overline{u' \zeta'}}_{V_{ezeta}} - \underbrace{\overline{w' \frac{\partial v'}{\partial z}}}_{V_{ev}} + \bar{F}_\lambda, \quad (3)$$

$$\underbrace{\frac{\partial \bar{u}}{\partial t}}_{U_t} = \underbrace{-\bar{u} \frac{\partial \bar{u}}{\partial r}}_{U_{mr}} - \underbrace{\left(u' \frac{\partial u'}{\partial r} + \frac{v'}{r} \frac{\partial u'}{\partial \lambda} \right)}_{U_{eh}} - \underbrace{\bar{w} \frac{\partial \bar{u}}{\partial z}}_{U_{mv}} - \underbrace{\overline{w' \frac{\partial u'}{\partial z}}}_{U_{ev}} + \underbrace{\frac{\bar{v}^2}{r} + f\bar{v} - \frac{1}{\rho} \frac{\partial \bar{p}}{\partial r}}_{U_{magf}} + \underbrace{\frac{v'^2}{r} - \frac{1}{\rho} \frac{\partial p'}{\partial r}}_{U_{eagf}} + \bar{F}_r, \quad (4)$$

where $\zeta = \left(\frac{1}{r} \frac{\partial(rv)}{\partial r} - \frac{1}{r} \frac{\partial u}{\partial \lambda} \right)$ is the vertical component of the relative vorticity; the overbar denotes the azimuthal average (mean); and the prime denotes the asymmetric portion (eddy) contributed by convective clouds and waves. The terms on the left-hand side of Equations 3 and 4 are the local rate of change of the azimuthal mean tangential (V_t) and radial (U_t) momentum, respectively. The five terms on the right-hand side of Equation (3) are the mean radial absolute vorticity flux (V_{mzeta}), the vertical advection of mean tangential momentum (V_{mv}), the eddy radial vorticity flux (V_{ezeta}), the vertical advection of eddy tangential momentum (V_{ev}), and the change of the mean tangential wind induced by three-dimensional (3D) subgrid-scale diffusion and PBL parametrization (\bar{F}_λ). The seven terms on the right-hand side of Equation (4), in sequence, are the radial advection of mean radial momentum (U_{mr}), the horizontal advection of eddy radial momentum (U_{eh}), the vertical advection of mean radial momentum (U_{mv}), the vertical advection of eddy radial momentum (U_{ev}), the imbalanced portion of the mean gradient wind forcing (U_{magf}), the eddy agradient forcing (U_{eagf}), and the mean radial wind change caused by 3D subgrid-scale diffusion and PBL parametrization (\bar{F}_r).

When we calculate the tangential and radial momentum budget terms in Equations 3 and 4, the mean-eddy fields are computed using storm-relative wind fields (i.e. a TC-comoving framework) by subtracting the storm's translation speed from the model winds. The storm's translation speeds are estimated using the storm's centroid locations defined earlier.

As noted by Persing *et al.* (2013) and Montgomery *et al.* (2020), we emphasize again that the eddy-mean partition used in this study may project localized convective updraughts onto both "mean" and "eddy" terms due to

the non-zero azimuthal average of localized perturbations. While the azimuthal average of localized perturbations is small in general and will not alter the conclusions, special attention is required to interpret results when perturbations are large and uneven in terms of positive versus negative values in any annulus.

3.3.2 | Tangential momentum budget analysis

The tendency and budget terms for the mean tangential wind are shown in Figure 6 for HRL and Figure 7 for LRL, averaged from 0900 UTC to 1500 UTC 30 July with 15 min data output. This time period is chosen because (a) the HRL-LRL differences in azimuthally symmetric and asymmetric kinetic energy are significant (i.e. in the region between the two red dashed lines in Figure 5) and (b) it is before the intensification rates diverge between the two experiments (Figure 2b,c). Note again that all time-averaged tendency terms are calculated following the storm's centre, meaning that the storm's movement of about 50 km in 6 hr during the period is subtracted from the wind fields. The effect of three-dimensional subgrid-scale diffusion and the PBL mixing (i.e. \bar{F}_λ) is one order of magnitude smaller than the other terms in Equation (3) and makes little contribution to the mean tangential wind changes; thus, this term is not shown. For the mean tangential wind tendency directly calculated from model output (Figures 6a and 7a; the left-hand-side term in Equation (3)), although the storm's circulation intensifies in both experiments, results from HRL and LRL are quite different. The maximum intensification rate of the mean tangential wind (orange shading) is stronger in HRL than in LRL, and it is located inside the RMW for HRL and outside for LRL. Note that the RMW is defined using 6-hourly averaged tangential wind speeds. LRL has only a weak-positive-tendency column existing in the inner core (eyewall) region of the storm. Within this inner core region, the maximum V_t in HRL is near the surface, while in LRL it is in the upper half of the column. Also, in LRL a weak negative-tendency column (located right inside the RMW) exists between the aforementioned weak intensification rate region inside the RMW and the maximum intensification rate region outside, while the negative tendency in HRL is near the centre of the storm (i.e. within the eye region). Compared to LRL, the greater intensification rate of the cyclonic circulation within the RMW in HRL is more favourable for the storm's intensification, which explains why its RI is stronger than that in LRL.

Although the sum of the tendency terms on the right-hand side of Equation (3) for HRL (Figure 6b) overestimates the model's actual tangential wind tendency in

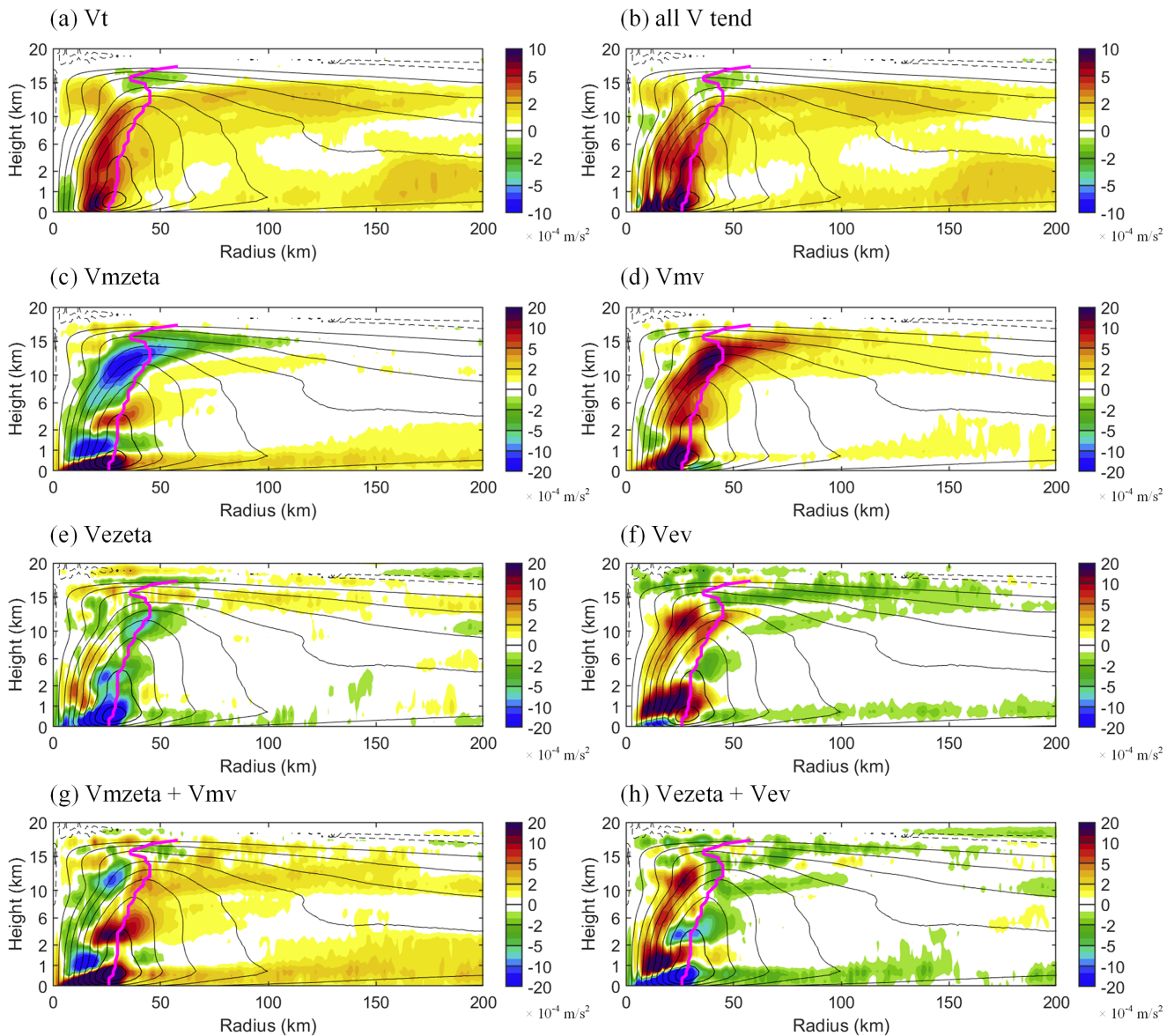


FIGURE 6 Radius–height plots of the 6-hourly and azimuthally averaged tangential momentum budget terms in Equation (3) for the HRL experiment from 0900 UTC to 1500 UTC 30 July 2011. (a) The mean tangential wind tendency (i.e. the left-hand side of Equation (3)), (b) the sum of all budget terms on the right-hand side of Equation (3). (c) the mean radial absolute vorticity flux (Vmzeta), (d) the vertical advection of mean tangential momentum (Vmv), (e) the eddy radial vorticity flux (Vezeta), (f) the vertical advection of eddy tangential momentum (Vev), (g) the summation of the mean processes (Vmzeta + Vmv), and (h) the summation of the eddy processes (Vezeta + Vev). The black contours are tangential winds and the pink lines connect the radii of maximum wind at all vertical levels. Note that the vertical coordinate below 2 km is expanded for better visualization [Colour figure can be viewed at wileyonlinelibrary.com]

both magnitude and coverage (the V_t term in Equation (3); Figure 6a), inside the RMW the momentum budget analysis can still be used to compare and diagnose the dominant processes that contribute to *Muifa's* intensity change during the early stage of RI. A similar overestimation is seen in LRL, though the differences within the RMW (Figure 7a,b) are smaller than those in HRL. The inconsistencies between Figure 6a,b and between Figure 7a,b are partly due to the errors introduced by using finite difference methods and potentially the inadequate WRF

output frequency (every 15 min), which cannot capture convection life cycles.

To diagnose the contributions of the tendency terms on the right-hand side of Equation (3), we start with the mean flow processes. Within the inner core region, the radial mean vorticity flux (Vmzeta) in HRL enhances the circulation very close to the surface and near the RMW between 2 and 5 km. It also reduces the circulation in a 1.5-km-thick layer above the boundary as well as between the middle and upper levels (Figure 6c), where air moves away

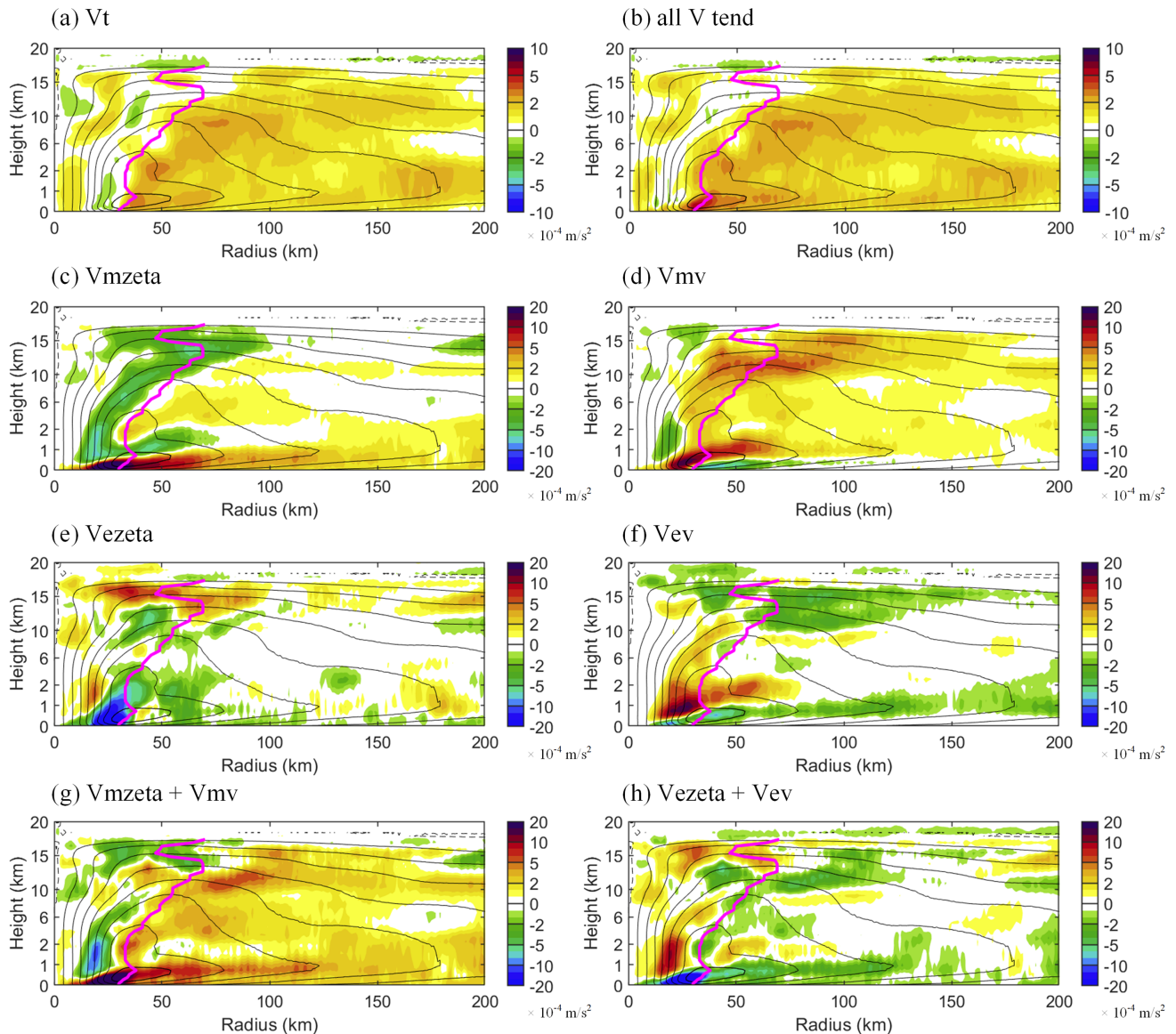


FIGURE 7 (a–h) Same as Figure 6 but for LRL [Colour figure can be viewed at wileyonlinelibrary.com]

from the storm's centre along the sloped eyewall. On the other hand, the vertical advection of mean tangential wind (V_{mv}) enhances the mean tangential circulation near the surface and right inside the eyewall (Figure 6d). The net effect (Figure 6g) produces negative tendencies right above the boundary layer and near the inner core, particularly between 10 and 15 km, and positive tendencies close to the surface and near the RMW between 2 and 10 km. Outside the RMW, the net mean flow effect produces positive tendencies overall, mostly resulting from the V_{mv} .

The eddy processes behave quite differently. In HRL, while the radial eddy vorticity flux (V_{ezeta}) weakens the mean tangential wind near the surface and along the RMW of the eyewall (Figure 6e), the vertical eddy advection term (V_{ev}) enhances the mean tangential wind in *Muifa's* inner core, along the upper part of the RMW region,

and in the lower troposphere (Figure 6f). Further analysis confirmed that the vertical velocity is particularly strong (i.e. convective storms) at the upper levels where V_{ev} is large (figure not shown). The net eddy effect (Figure 6h), which is in general opposite to the net mean flow effect (Figure 6g), dominates the azimuthal mean tangential wind tendency near the inner part of the eyewall (within a 20 km radius). This is consistent with the result of Montgomery *et al.* (2020). In contrast, outside the RMW, the mean flow effect dominates the net eddy effect (Figure 6b). A similar overall conclusion is obtained in LRL (Figure 7), but there are important differences: (1) the effects of eddy and mean momentum processes almost cancel inside the RMW, except close to the TC centre region (i.e. the weak-positive-tendency column in Figure 7a,b), where the net mean flow effect slightly dominates the eddy

contribution, (2) the maximum positive mean tangential wind tendency in LRL extends farther outward from the RMW (radius greater than 50 km), as discussed before, and is mainly driven by V_{mv} and, to a lesser extent, by V_{mzeta} , and (3) in LRL, between 2 and 10 km the mean vertical advection term (V_{mv}) outside the RMW is clearly greater than the radial mean vorticity flux (V_{mzeta}), while in HRL the difference is not as pronounced.

The above mean tangential momentum budget analysis between HRL and LRL indicates that eddy processes in the inner core of the storm are the main driver of the storm's intensification and eyewall contraction during early RI, which is expected to be more consistent with what happens in reality. A resolution of 1 km or higher is required to properly resolve the eddy effect. Outside the RMW, the mean processes make the greatest contribution to the mean tendencies in both HRL and LRL, mostly driven by vertical advection and aided by the radial mean vorticity flux. We note that while the large-scale environment is not examined here, favourable environmental conditions, such as high surface moisture entropy fluxes over the ocean, are required regardless of which processes dominate.

3.3.3 | The radial momentum budget analysis

Figures 8 and 9 show the azimuthally averaged budget terms of the mean radial wind for HRL and LRL, respectively, during the same period as in the tangential momentum budget analysis. Compared to the tangential momentum budget in Equation (3), the tendencies directly calculated from WRF outputs (U_t ; Figures 8a and 9a) and the summation of the right-hand-side terms (Figures 8b and 9b) of Equation (4) are more consistent. Figure 8c shows that over the storm area, the mean gradient wind imbalance state (U_{magf} ; the departure from the mean gradient wind balance, i.e. $\frac{v^2}{r} + f\bar{v} - \frac{1}{\rho} \frac{\partial \bar{p}}{\partial r} \neq 0$) in HRL produces negative mean radial wind tendencies in the lower-to-middle troposphere (1–7 km height), which enhance the inflow over this region. On the other hand, U_{magf} produces positive mean radial wind tendencies within the boundary layer and in the middle-to-upper troposphere (8–15 km height), which weaken the boundary layer and middle-to-upper-layer inflow (below the maximum vertical velocity in Figure 4g) and enhance upper-level outflow over the eyewall region (Figure 8c). These results are consistent with those in Montgomery *et al.* (2020). For LRL, although similar results are obtained, the positive tendency in the upper troposphere extends farther outward (Figure 8a versus 9a) and a negative tendency band exists between 5 and 10 km outside

the RMW. The tendencies are overall greater and more concentrated toward the storm centre in HRL than in LRL. The evident dipole-pattern in U_{magf} in the lower (negative) and upper (positive) layers of the TC's inner core in HRL and LRL suggests that U_{magf} is an important driver of the TC's vertical circulation intensification, in particular over the middle–upper troposphere (Figure 8a versus 8c and Figure 9a versus 9c). The total horizontal eddy contribution ($U_{eagf} + U_{eh}$) largely compensates the radial wind changes induced by the mean gradient wind imbalance (U_{magf}) in the lower-to-middle layer in both HRL and LRL (Figures 8d and 9d). Our results indicate that the use of 1 km resolution does not increase the ratio of the contribution of the horizontal eddy transfer processes to the secondary circulation intensification during *Muifa's* early RI.

For the remaining terms in the azimuthally averaged radial momentum budget equation of Equation (4), the horizontal (U_{mv} ; Figures 8e and 9e) and vertical (U_{mr} ; Figures 8g and 9g) mean flow advection terms together (i.e. $U_{mv} + U_{mr}$; Figures 8h and 9h) mainly enhance the inflow below the upper-level outflow, and this effect is largely offset by U_{magf} over *Muifa's* upper eyewall region. The vertical advection of eddy radial momentum, U_{ev} (Figures 8f and 9f), is relatively small compared to the other processes. We note again that the three-dimensional diffusion and PBL term, \overline{F}_r , is one order of magnitude smaller than the other terms in Equation (4), so it is not shown here.

The mean radial momentum budget analysis indicates that the radial wind tendency U_t in both HRL (Figure 8a) and LRL (Figure 9a) is mainly driven by the combined mean effect of U_{magf} , U_{mv} and U_{mr} (Figures 8b,c,e,g and 9b,c,e,g). Unlike the mean tangential wind, the use of a 1 km resolution does not alter the dominant mechanisms, but, as expected, individual tendency terms become stronger and shift upward and toward the centre of the storm when a higher resolution is used. When the model resolution is increased from 3 to 1 km, why are the dominant processes different for the tangential wind acceleration but not for the radial wind? We suspect that this is because the contribution of convection to the mean tangential wind (circulation) acceleration becomes more efficient inside the RMW than outside when it is better resolved in HRL, but the same is not true for the mean radial wind acceleration. Further investigation is needed, and we leave it for future work.

3.4 | The TC–ocean coupling effect

We wonder if coupled ocean–atmosphere processes may interfere with the impacts of resolution described above. By excluding the TC-induced SST cooling feedback, the

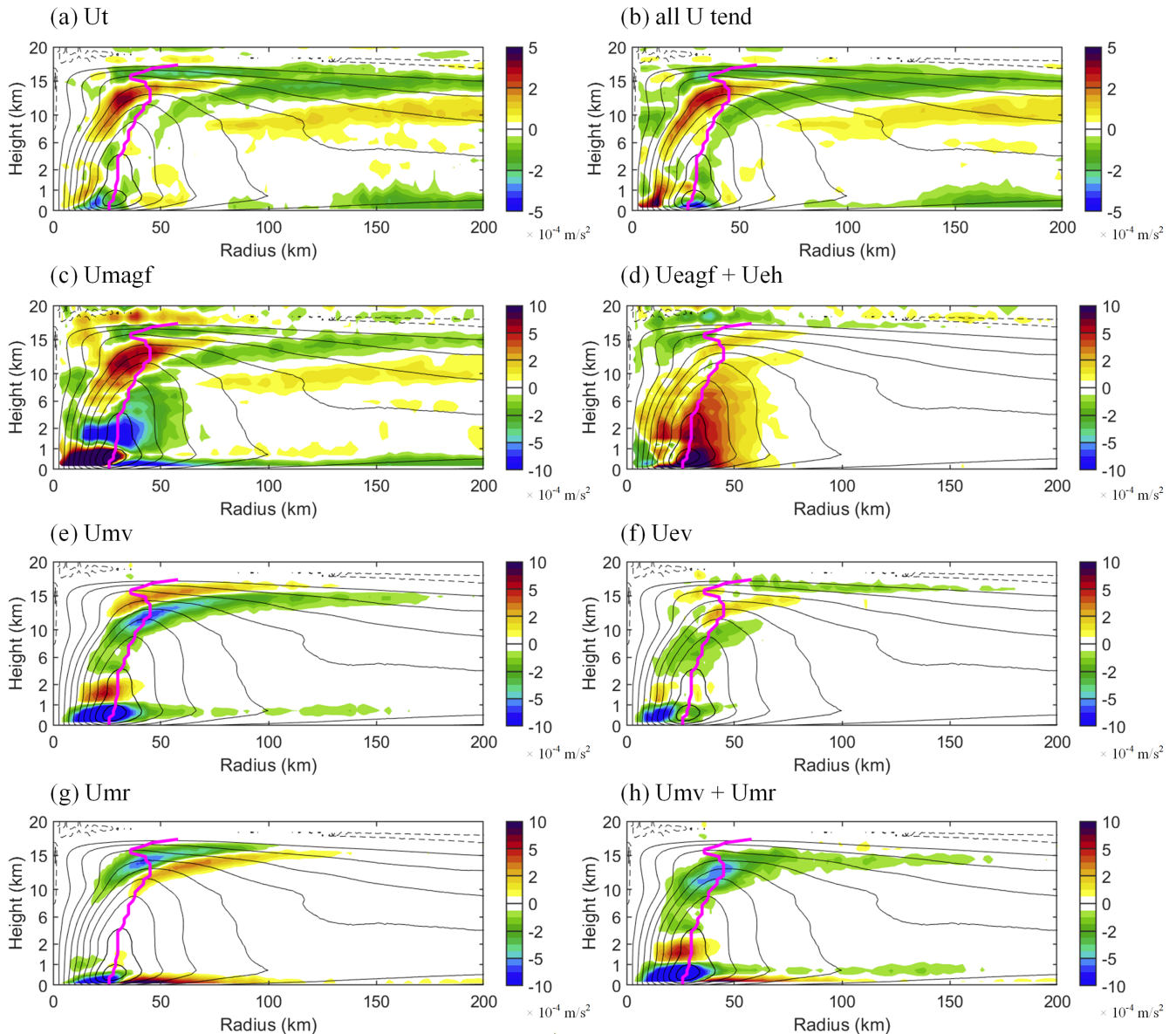


FIGURE 8 Radius–height plots of the 6 hr averaged values of the azimuthally-averaged radial momentum budget terms in Equation (4) for the HRL experiment from 0900 UTC to 1500 UTC 30 July 2011. (a) Is the mean radial wind tendency (i.e. the left-hand side of Equation (4)). (b) is the sum of all budget terms on the right-hand side of Equation (4), (c) the imbalanced portion of the mean gradient wind forcing (U_{magf}), (d) the summation of the eddy gradient forcing (U_{eagf}) and the horizontal advection of eddy radial momentum (U_{eh}), (e) the vertical advection of mean radial momentum (U_{mv}), (f) the vertical advection of eddy radial momentum (U_{ev}), (g) the radial advection of mean radial momentum (U_{mr}), and (h) the summation of U_{mv} and U_{mr} . The black contours are tangential winds and the pink lines connect the radii of maximum wind at all vertical levels. Note that the vertical coordinate below 2 km is expanded for better visualization [Colour figure can be viewed at wileyonlinelibrary.com]

NoTCFB experiment with a 3 km resolution can produce a storm with an intensity similar to that in HRL in terms of the MSLP and maximum 10 m wind, though RI is slightly delayed in time (Figure 2b,c). Among these three experiments, the eyewall in NoTCFB (figure not shown) is located farthest outward (~ 40 – 50 km), and the maximum mean radial and tangential winds during the early RI period are the strongest (figure not shown), enabling it to

sustain an intensity that is similar to that in HRL. Figure 10 shows the same azimuthally averaged momentum budget terms for the mean tangential wind equation for NoTCFB. Unlike HRL and LRL, the mean tangential wind tendency calculated from the left-hand-side term (Figure 10a) and the summation of the right-hand-side terms of Equation (3) (Figure 10b) are quite similar within the RMW. Similar to LRL, the maximum positive tendencies in NoTCFB are

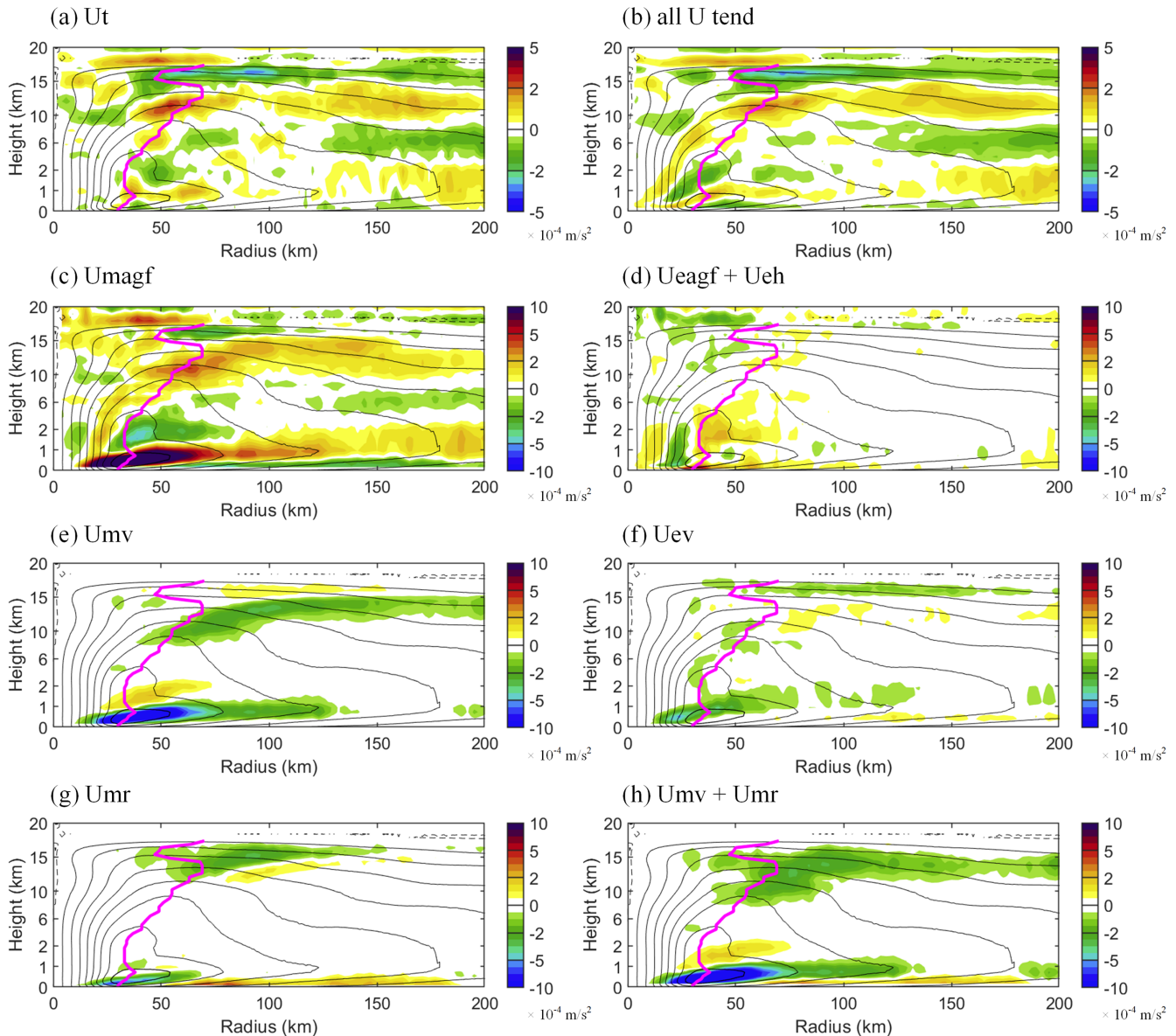


FIGURE 9 (a–h) Same as Figure 8 but for LRL [Colour figure can be viewed at wileyonlinelibrary.com]

located outside the RMW (indicated by pink lines) except in the bottom 2 km of the atmosphere, where the maximum tendency is located inside the RMW. However, as expected, the magnitudes in NoTCFB are larger, and they extend up to 15 km. Similar to HRL, NoTCFB has negative tendencies within the eye in the lower troposphere and is deeper (Figure 6a versus 10a). However, unlike the other two experiments, the tendencies within the RMW above 7 km are all negative in NoTCFB.

The NoTCFB azimuthal mean tangential momentum budget, averaged from 0900 UTC to 1500 UTC 30 July, is now analysed. Results show that the mean flow effects dominate the eddy effects near the centre of the storm (negative), near the surface (positive), and between 3 and 14 km (positive) in NoTCFB (Figure 10c,d,g). On the other

hand, the eddy effects dominate the positive tendencies near the upper part of the outflow outside the RMW and at the top of the boundary layer. Thus, while HRL and NoTCFB produce similar maximum intensities, the dominant processes driving the mean circulation intensification are different, and their maximum tangential momentum tendencies are not collocated (inside versus outside the RMW). The exception is close to the surface, where both are located inside the RMW and are dominated by the mean processes during early RI. Comparing LRL and NoTCFB, the dominant processes for the mean circulation intensification are similar except near the top of the storm, where the eddy terms play an important role in NoTCFB but not in LRL. In NoTCFB, the eddy effect at this level is mainly driven by waves (figure not

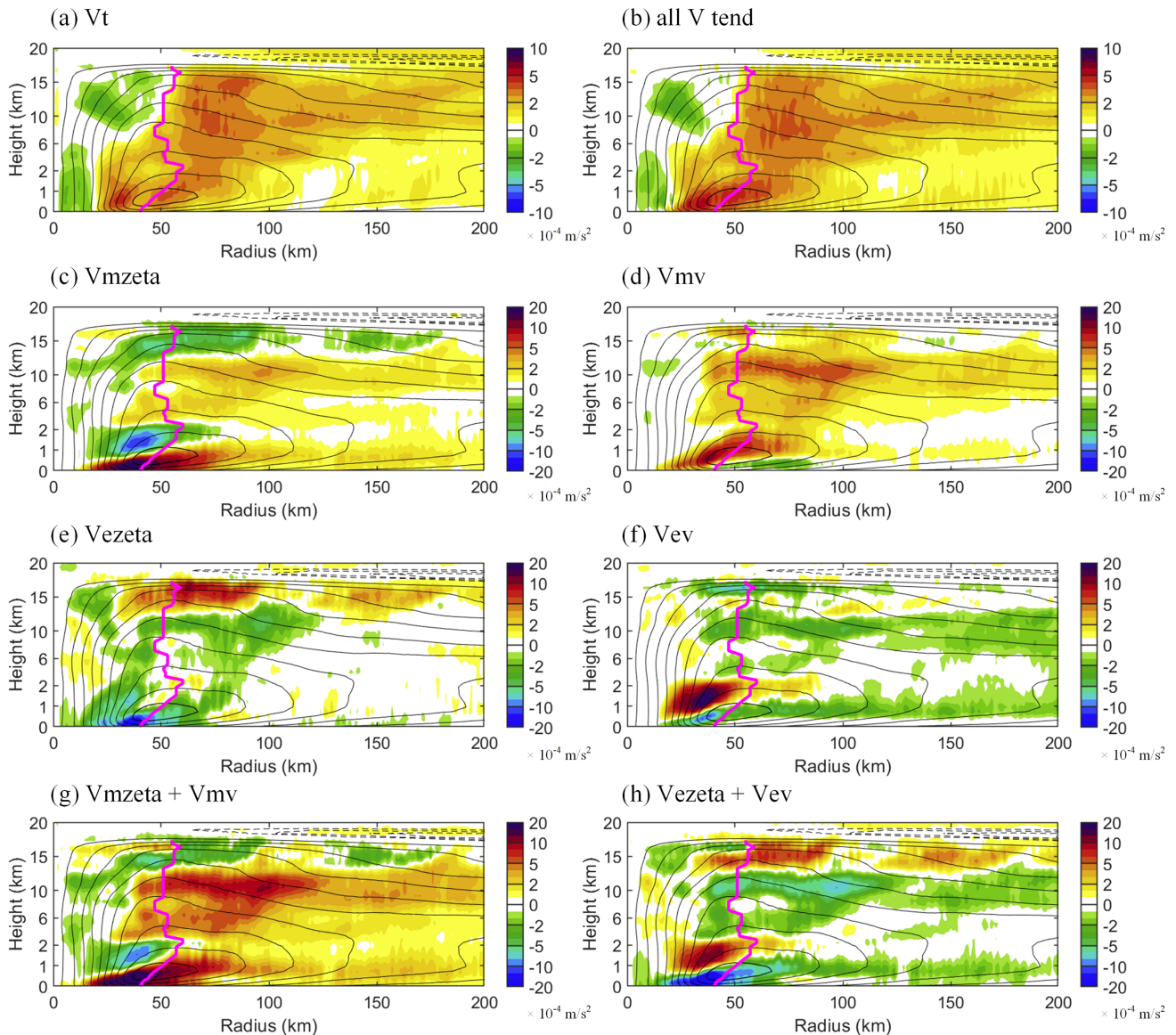


FIGURE 10 (a–h) Same as Figure 6 but for NoTCFB [Colour figure can be viewed at wileyonlinelibrary.com]

shown). We speculate that it is due to the shear instability of the strong mean flow at upper levels in NoTCFB (figure not shown), since both horizontal ($\partial\bar{v}/\partial r$) and vertical ($\partial\bar{v}/\partial z$) wind shears at upper levels are much stronger in NoTCFB than in LRL. Further investigation is required in the future. For the mean radial momentum budget in NoTCFB, the dominant processes are in general very similar to those in HRL and LRL (figure not shown), except that their patterns can be different, including shifts in location.

4 | SUMMARY AND CONCLUSIONS

While TC intensity forecasts have improved in the past two decades, challenges remain, especially for RI.

Even when TC RI is reasonably forecasted, are the dominant processes responsible for intensification correctly captured by numerical models? Without reasonably representing these processes, it is difficult to accurately predict the intensity of a storm that experiences both rapid intensification and weakening during its life cycle.

This study aims to determine the dominant mean and eddy momentum transfer processes that are responsible for RI and investigate how those processes may change with model spatial resolution and TC-induced SST cooling feedback. Super-typhoon *Muifa*, which occurred over the western North Pacific from late July to early August in 2011, is used as a case-study. A fully coupled atmosphere–ocean WRF-ROMS model is used for simulations. Two numerical experiments are conducted

with different horizontal grid spacing in WRF: 1 km (HRL) versus 3 km (LRL). A third experiment is the same as LRL but without TC-induced SST cooling feedback (NoTCFB).

The HRL experiment with a 1 km resolution can better resolve convection, allowing it to reasonably reproduce *Muifa's* rapid intensification and weakening and its morphology during rapid intensification. When the resolution is reduced to 3 km, LRL still captures *Muifa's* life cycle but underestimates its maximum intensity by 15 hPa in MSLP and 11 m s^{-1} in the maximum 10 m wind, meaning weaker rapid intensification and weakening rates. After further removing the TC-induced SST cooling effect, NoTCFB (with a 3 km resolution) is capable of reproducing *Muifa's* rapid intensification, but the rapid weakening becomes too weak compared to HRL, suggesting inappropriate dynamics caused by wrongly simulated surface energy fluxes.

The azimuthally averaged wind circulation from 0600 UTC to 1800 UTC 30 July during early RI is compared between HRL and LRL. Their wind patterns are similar, including the maximum cyclonic circulation at the top of the boundary layer, strong inward radial winds within the boundary layer, and strong outward radial winds at upper levels. The dipole patterns in their wind differences result from the stronger intensity in the inner core (eyewall) region in HRL but greater intensity outside the eyewall in LRL, as well as the upward and inward shifts of the eyewall in HRL.

The differences in azimuthally averaged K_m and K_e (symmetric and asymmetric kinetic energy, respectively) between HRL and LRL show that before 1800 UTC 30 July, HRL has 10 J m^{-2} higher K_m within a 50 km radius and 5 J m^{-2} lower K_m outside. For the eddy kinetic energy, HRL has 10 J m^{-2} higher K_e in *Muifa's* inner core, which is located within the radius of the maximum positive K_m differences.

Azimuthally averaged tangential and radial momentum budget analyses are performed to determine the contributions of mean and eddy momentum transfer to *Muifa's* early RI before the TC intensity diverges between HRL and LRL. For the mean tangential wind, the maximum local rates of change (i.e. V_t in Equation (1)) among the three experiments are distinct. HRL has the maximum positive tendency located inside the RMW, while LRL and NoTCFB have the maximum tendencies outside the RMW. Additionally, the maximum positive tendency has a larger area and greater magnitude in NoTCFB than in LRL. For HRL, the net eddy effect dominates the net mean flow effect in driving the acceleration of the mean circulation inside the RMW, and this is favourable for TC intensification and eyewall contraction. The net eddy effect is mainly driven by vertical advection of eddy tangential momentum

at middle to upper levels and eddy radial vorticity flux at low levels. In contrast, over the same region inside the RMW, the mean and eddy effects almost cancel each other in both LRL and NoTCFB, except near the surface. Outside the RMW, the net mean flow effect dominates the net eddy effect for all three experiments, in which HRL has the weakest magnitude and NoTCFB has the strongest. The primary contributor to the net mean flow effect outside the RMW is the vertical advection of mean tangential momentum. For the mean radial momentum analysis, although the patterns of local rates of change show some discrepancies among the three experiments, their dominant processes in general agree well with each other and are mainly driven by the combined effect of the mean gradient wind imbalance and the horizontal and vertical mean flow advection.

Results from this study indicate that a 1 km model resolution is required not only to better resolve eddy processes, including convective cells, but also to ensure the proper role and location of dominant processes (mean versus eddy) in momentum transfer during RI. In addition, the feedback from TC-induced SST cooling is critical for capturing *Muifa's* rapid weakening. Montgomery and Smith (2017) discussed four main paradigms for TC intensification: conditional instability of the second kind (CISK), cooperative intensification, wind-induced surface heat exchange (WISHE), and rotating convection. For HRL, our analysis found that the vertical eddy advection term ($V_{ev} = -\overline{w'\partial v'/\partial z}$) is a dominant eddy process and convection is active in regions where V_{ev} is large, which is supportive of the rotating convection paradigm. However, RI occurs under favourable environment conditions, such as high surface moist entropy fluxes, in addition to storm-scale dynamics and thermodynamics. This study also emphasizes that under favourable environmental conditions, without using a 1 km or higher resolution, the role of eddy processes in TC intensification may be underestimated and the dominant processes are not correctly represented. Finally, we note that our conclusions are based on one case-study and that more cases should be conducted to ensure the robustness of the conclusions.

AUTHOR CONTRIBUTIONS


Yang Yu: Formal analysis; methodology; visualization; writing – original draft. **Shu-Hua Chen:** Formal analysis; supervision; writing – original draft; writing – review and editing. **Yu-Heng Tseng:** Formal analysis; visualization; writing – review and editing. **Gregory Foltz:** Visualization; writing – review and editing. **Rong-Hua Zhang:** Writing – review and editing. **Huiwang Gao:** Writing – review and editing.

ACKNOWLEDGEMENTS

The authors thank Michael T. Montgomery and another anonymous reviewer for their constructive suggestions and comments. The authors would also like to thank the COAWST team for the development of the model. The COAWST model is available at <https://www.usgs.gov/centers/whcmssc/science/coawst-coupled-ocean-atmosphere-wave-sediment-transport-modeling-system>. Several data sources were used in this study: FNL data from <https://rda.ucar.edu/datasets/ds083.2/>; HYCOM reanalysis from <https://www.hycom.org/dataserver/gofs-3pt1/reanalysis>; CMA best track data from https://tcdata.typhoon.org.cn/zjljsjj_zlhq.html; and MTSAT2 images from <https://www.ncdc.noaa.gov/hursat/index.php?name=b1-access>. Y. Yu was supported by the China Scholarship Council (CSC) when he visited University of California Davis. S.-H. Chen was supported by NSF grant 1,624,414–0. G. Foltz was supported by base funds to NOAA/AOML. R.-H. Zhang was supported by the Special Funds of Shandong Province for Pilot National Laboratory for Marine Science and Technology (Qingdao; Grant No. 2022QNLM0103014) and the Startup Foundation for Introducing Talent of NUIST.

ORCID

Yang Yu  <https://orcid.org/0000-0002-5527-1540>

Shu-Hua Chen  <https://orcid.org/0000-0001-5929-1074>

REFERENCES

- Aberson, S.D. (2001) The ensemble of tropical cyclone track forecasting models in the North Atlantic Basin (1976–2000). *Bulletin of the American Meteorological Society*, 82, 1895–1904. [https://doi.org/10.1175/1520-0477\(2001\)082<0000:TEOTCT>2.3.CO;2](https://doi.org/10.1175/1520-0477(2001)082<0000:TEOTCT>2.3.CO;2).
- Bhalachandran, S., Chavas, D.R., Marks, F.D., Dubey, S., Shreevastava, A. and Krishnamurti, T.N. (2020) Characterizing the energetics of vortex-scale and sub-vortex-scale asymmetries during tropical cyclone rapid intensity changes. *Journal of the Atmospheric Sciences*, 77, 315–336. <https://doi.org/10.1175/JAS-D-19-0067.1>.
- Booij, N., Ris, R.C. and Holthuijsen, L.H. (1999) A third-generation wave model for coastal regions 1. Model description and validation. *J. Geophys. Res. Ocean.*, 104, 7649–7666. <https://doi.org/10.1029/98JC02622>.
- Bye, J.A.T. and Wolff, J.O. (1999) Atmosphere-ocean momentum exchange in general circulation models. *Journal of Physical Oceanography*, 29, 671–692. [https://doi.org/10.1175/1520-0485\(1999\)029<0671:AOMEIG>2.0.CO;2](https://doi.org/10.1175/1520-0485(1999)029<0671:AOMEIG>2.0.CO;2).
- Chan, J.C.L. (2005) The physics of tropical cyclone motion. *Annual Review of Fluid Mechanics*, 37, 99–128. <https://doi.org/10.1146/annurev.fluid.37.061903.175702>.
- Chan, J.C.L., Duan, Y. and Shay, L.K. (2001) Tropical cyclone intensity change from a simple ocean-atmosphere coupled model. *Journal of the Atmospheric Sciences*, 58, 154–172. [https://doi.org/10.1175/1520-0469\(2001\)058<0154:TCICFA>2.0.CO;2](https://doi.org/10.1175/1520-0469(2001)058<0154:TCICFA>2.0.CO;2).
- Chang, Y.P., Yang, S.C., Lin, K.J., Lien, G.Y. and Wu, C.M. (2020) Impact of tropical cyclone initialization on its convection development and intensity: A case study of typhoon megi (2010). *Journal of the Atmospheric Sciences*, 77, 443–464. <https://doi.org/10.1175/JAS-D-19-0058.1>.
- Chen, S.-H. and Sun, W.-Y. (2002) A one-dimensional time dependent cloud model. *J. Meteorol. Soc. Japan. Ser. II*, 80, 99–118. <https://doi.org/10.2151/jmsj.80.99>.
- Chih, C.-H. and Wu, C.-C. (2020) Exploratory analysis of western heat content and sea surface temperature underlying tropical cyclone rapid intensification in the Western North Pacific. *Journal of Climate*, 33, 1031–1050. <https://doi.org/10.1175/JCLI-D-19-0305.1>.
- Črnivec, N., Smith, R.K. and Kilroy, G. (2016) Dependence of tropical cyclone intensification rate on sea-surface temperature. *Quarterly Journal of the Royal Meteorological Society*, 142, 1618–1627. <https://doi.org/10.1002/qj.2752>.
- Dare, R.A. and McBride, J.L. (2011) Sea surface temperature response to tropical cyclones. *Monthly Weather Review*, 139, 3798–3808. <https://doi.org/10.1175/MWR-D-10-05019.1>.
- Davis, C.A. and Low-Nam, S. (2001) The NCAR-AFWA tropical cyclone bogussing scheme. *Air Force Weather Agency Rep*, 12, 1–13.
- DeMaria, M. and Kaplan, J. (1994) Sea surface temperature and the maximum intensity of Atlantic tropical cyclones. *Journal of Climate*, 7, 1324–1334. [https://doi.org/10.1175/1520-0442\(1994\)007<1324:SSTATM>2.0.CO;2](https://doi.org/10.1175/1520-0442(1994)007<1324:SSTATM>2.0.CO;2).
- DeMaria, M., Knaff, J.A. and Sampson, C. (2007) Evaluation of long-term trends in tropical cyclone intensity forecasts. *Meteorology and Atmospheric Physics*, 97, 19–28. <https://doi.org/10.1007/s00703-006-0241-4>.
- DeMaria, M., Sampson, C.R., Knaff, J.A. and Musgrave, K.D. (2014) Is tropical cyclone intensity guidance improving? *Bulletin of the American Meteorological Society*, 95, 387–398. <https://doi.org/10.1175/BAMS-D-12-00240.1>.
- Dong, L. and Zhang, F. (2016) OBEST: an observation-based ensemble subsetting technique for tropical cyclone track prediction. *Weather and Forecasting*, 31, 57–70. <https://doi.org/10.1175/WAF-D-15-0056.1>.
- Egbert, G.D. and Erofeeva, S.Y. (2002) Efficient inverse modeling of barotropic ocean tides. *Journal of Atmospheric and Oceanic Technology*, 19, 183–204.
- Egbert, G.D., Bennett, A.F. and Foreman, M.G.G. (1995) TOPEX/POSEIDON tides estimated using a global inverse model. *J. Geophys. Res. Ocean.*, 99, 24821–24852.
- Emanuel, K.A. (1999) Thermodynamic control of hurricane intensity. *Nature*, 401, 665–669. <https://doi.org/10.1038/44326>.
- Fairall, C.W., Bradley, E.F., Godfrey, J.S., Wick, G.A., Edson, J.B. and Young, G.S. (1996a) Cool-skin and warm-layer effects on sea surface temperature. *J. Geophys. Res. Ocean.*, 101, 1295–1308. <https://doi.org/10.1029/95JC03190>.
- Fairall, C.W., Bradley, E.F., Rogers, D.P., Edson, J.B. and Young, G.S. (1996b) Bulk parameterization of air-sea fluxes for tropical ocean-global atmosphere Coupled-Ocean atmosphere response experiment. *J. Geophys. Res. Ocean.*, 101, 3747–3764.
- Fairall, C.W., Bradley, E.F., Hare, J.E., Grachev, A.A. and Edson, J.B. (2003) Bulk parameterization of air sea fluxes: updates and verification for the COARE algorithm. *Journal of Climate*, 16, 571–591.

- Fang, J. and Zhang, F. (2011) Evolution of multiscale vortices in the development of hurricane Dolly (2008). *Journal of the Atmospheric Sciences*, 68, 103–122. <https://doi.org/10.1175/2010JAS3522.1>.
- Foltz, G.R., Balaguru, K. and Hagos, S. (2018) Interbasin differences in the relationship between SST and tropical cyclone intensification. *Monthly Weather Review*, 146, 853–870. <https://doi.org/10.1175/MWR-D-17-0155.1>.
- Franklin, J.L., McAdie, C.J. and Lawrence, M.B. (2003) Trends in track forecasting for tropical cyclones threatening the United States, 1970–2001. *Bulletin of the American Meteorological Society*, 84, 1197–1204. <https://doi.org/10.1175/BAMS-84-9-1197>.
- Fudeyasu, H., Ito, K. and Miyamoto, Y. (2018) Characteristics of tropical cyclone rapid intensification over the western North Pacific. *Journal of Climate*, 31, 8917–8930. <https://doi.org/10.1175/JCLI-D-17-0653.1>.
- Gopalakrishnan, S.G., Marks, F., Zhang, X., Bao, J.W., Yeh, K.S. and Atlas, R. (2011) The experimental HWRF system: a study on the influence of horizontal resolution on the structure and intensity changes in tropical cyclones using an idealized framework. *Monthly Weather Review*, 139, 1762–1784. <https://doi.org/10.1175/2010MWR3535.1>.
- Gopalakrishnan, S.G., Goldenberg, S., Quirino, T., Zhang, X., Marks, F., Yeh, K.S., Atlas, R. and Tallapragada, V. (2012) Toward improving high-resolution numerical hurricane forecasting: influence of model horizontal grid resolution, initialization, and physics. *Weather and Forecasting*, 27, 647–666. <https://doi.org/10.1175/WAF-D-11-00055.1>.
- Hendricks, E.A., Peng, M.S., Fu, B. and Li, T. (2010) Quantifying environmental control on tropical cyclone intensity change. *Monthly Weather Review*, 138, 3243–3271. <https://doi.org/10.1175/2010MWR3185.1>.
- Holliday, C.R. and Thompson, A.H. (1979) Climatological characteristics of rapidly intensifying typhoons. *Monthly Weather Review*, 107, 1022–1034. [https://doi.org/10.1175/1520-0493\(1979\)107<1022:CCORIT>2.0.CO;2](https://doi.org/10.1175/1520-0493(1979)107<1022:CCORIT>2.0.CO;2).
- Hsiao, L.F., Chen, D.S., Hong, J.S., Yeh, T.C. and Fong, C.T. (2020) Improvement of the numerical tropical cyclone prediction system at the Central Weather Bureau of Taiwan: TWRF (typhoon WRF). *Atmosphere (Basel)*, 11, 657. <https://doi.org/10.3390/atmos11060657>.
- Iacono, M.J., Delamere, J.S., Mlawer, E.J., Shephard, M.W., Clough, S.A. and Collins, W.D. (2008) Radiative forcing by long-lived greenhouse gases: calculations with the AER radiative transfer models. *Journal of Geophysical Research*, 113, D13103. <https://doi.org/10.1029/2008JD009944>.
- Jacob, R., Larson, J. and Ong, E. (2005) $M \times N$ communication and parallel interpolation in Community Climate System Model version 3 using the model coupling toolkit. *International Journal of High Performance Computing Applications*, 19, 293–307. <https://doi.org/10.1177/1094342005056116>.
- Jiménez, P.A., Dudhia, J., González-Rouco, J.F., Navarro, J., Montávez, J.P. and García-Bustamante, E. (2012) A revised scheme for the WRF surface layer formulation. *Monthly Weather Review*, 140, 898–918. <https://doi.org/10.1175/MWR-D-11-00056.1>.
- Jin, H., Peng, M.S., Jin, Y. and Doyle, J.D. (2014) An evaluation of the impact of horizontal resolution on tropical cyclone predictions using COAMPS-TC. *Weather and Forecasting*, 29, 252–270. <https://doi.org/10.1175/WAF-D-13-00054.1>.
- Jones, P.W. (1999) First- and second-order conservative remapping schemes for grids in spherical coordinates. *Monthly Weather Review*, 127, 2204–2210. [https://doi.org/10.1175/1520-0493\(1999\)127<2204:FASOCR>2.0.CO;2](https://doi.org/10.1175/1520-0493(1999)127<2204:FASOCR>2.0.CO;2).
- Judt, F. and Chen, S.S. (2016) Predictability and dynamics of tropical cyclone rapid intensification deduced from high-resolution stochastic ensembles. *Monthly Weather Review*, 144, 4395–4420. <https://doi.org/10.1175/MWR-D-15-0413.1>.
- Judt, F., Chen, S.S. and Berner, J. (2016) Predictability of tropical cyclone intensity: scale-dependent forecast error growth in high-resolution stochastic kinetic-energy backscatter ensembles. *Quarterly Journal of the Royal Meteorological Society*, 142, 43–57. <https://doi.org/10.1002/qj.2626>.
- Kain, J.S. (2004) The Kain–Fritsch convective parameterization: an update. *Journal of Applied Meteorology*, 43, 170–181. [https://doi.org/10.1175/1520-0450\(2004\)043<0170:TKCPAU>2.0.CO;2](https://doi.org/10.1175/1520-0450(2004)043<0170:TKCPAU>2.0.CO;2).
- Kanada, S., Tsujino, S., Aiki, H., Yoshioka, M.K., Miyazawa, Y., Tsuboki, K. and Takayabu, I. (2017) Impacts of SST patterns on rapid intensification of typhoon Megi (2010). *Journal of Geophysical Research—Atmospheres*, 122, 13245–13262. <https://doi.org/10.1002/2017JD027252>.
- Kaplan, J. and DeMaria, M. (2003) Large-scale characteristics of rapidly intensifying tropical cyclones in the North Atlantic basin. *Weather and Forecasting*, 18, 1093–1108. [https://doi.org/10.1175/1520-0434\(2003\)018<1093:LCORIT>2.0.CO;2](https://doi.org/10.1175/1520-0434(2003)018<1093:LCORIT>2.0.CO;2).
- Kaplan, J. and Coauthors. (2015) Evaluating environmental impacts on tropical cyclone rapid intensification predictability utilizing statistical models. *Weather and Forecasting*, 30, 1374–1396. <https://doi.org/10.1175/WAF-D-15-0032.1>.
- Kilroy, G. and Smith, R.K. (2016) A numerical study of deep convection in tropical cyclones. *Quarterly Journal of the Royal Meteorological Society*, 142, 3138–3151. <https://doi.org/10.1002/qj.2895>.
- Landsea, C.W. and Cangialosi, J.P. (2018) Have we reached the limits of predictability for tropical cyclone track forecasting? *Bulletin of the American Meteorological Society*, 99, 2237–2243. <https://doi.org/10.1175/BAMS-D-17-0136.1>.
- Larson, J., Jacob, R. and Ong, E. (2005) The model coupling toolkit: a new Fortran90 toolkit for building multiphysics parallel coupled models. *International Journal of High Performance Computing Applications*, 19, 277–292. <https://doi.org/10.1177/1094342005056115>.
- Leroux, M.-D. and Coauthors. (2018) Recent advances in research and forecasting of tropical cyclone track, intensity, and structure at landfall. *Tropical Cyclone Research and Review*, 7, 85–105. <https://doi.org/10.6057/2018TCRR02.02>.
- Li, G., Curcic, M., Iskandarani, M., Chen, S.S. and Knio, O.M. (2019) Uncertainty propagation in coupled atmosphere-wave-ocean prediction system: a study of hurricane Earl (2010). *Monthly Weather Review*, 147, 221–245. <https://doi.org/10.1175/MWR-D-17-0371.1>.
- Lin, I.-I., Wu, C.-C. and Pun, I.-F. (2008) Upper-ocean thermal structure and the western North Pacific category 5 typhoons. Part I: ocean features and the category 5 typhoons' intensification. *Mon. Wea. Rev.*, 136, 3288–3306.
- Lin, I.I., Pun, I.-F. and Wu, C.-C. (2009) Upper-ocean thermal structure and the western North Pacific category 5 typhoons. Part II: dependence on translation speed. *Mon. Wea. Rev.*, 137, 3744–3757.

- Liu, Y. and Coauthors. (2008) The operational mesogamma-scale analysis and forecast system of the U.S. Army test and evaluation command. Part I: overview of the modeling system, the forecast products, and how the products are used. *Journal of Applied Meteorology and Climatology*, 47, 1077–1092. <https://doi.org/10.1175/2007JAMC1653.1>.
- Malkus, J.S. and Riehl, H. (1960) On the dynamics and energy transformations in steady-state hurricanes. *Tellus*, 12, 1–20. <https://doi.org/10.3402/tellusa.v12i1.9351>.
- Mellor, G.L. and Yamada, T. (1982) Development of a turbulent closure model for geophysical fluid problems. *Review of Geophysics*, 20, 851–875.
- Miguez-Macho, G., Stenchikov, G.L. and Robock, A. (2004) Spectral nudging to eliminate the effects of domain position and geometry in regional climate model simulations. *Journal of Geophysical Research*, 109, 1–15. <https://doi.org/10.1029/2003JD004495>.
- Montgomery, M. T. and Smith, R. K. (2017) Recent developments in the fluid dynamics of tropical cyclones. *Annual Review of Fluid Mechanics*, 49, 541–574.
- Montgomery, M.T., Nicholls, M.E., Cram, T.A. and Saunders, A.B. (2006) A vortical hot tower route to tropical cyclogenesis. *Journal of the Atmospheric Sciences*, 63, 355–386. <https://doi.org/10.1175/JAS3604.1>.
- Montgomery, M.T., Kilroy, G., Smith, R.K. and Črnivec, N. (2020) Contribution of mean and eddy momentum processes to tropical cyclone intensification. *Quarterly Journal of the Royal Meteorological Society*, 146(732) qj.3837, 3101–3117. <https://doi.org/10.1002/qj.3837>.
- Nguyen, L.T., Molinari, J. and Thomas, D. (2014) Evaluation of tropical cyclone center identification methods in numerical models. *Monthly Weather Review*, 142, 4326–4339. <https://doi.org/10.1175/MWR-D-14-00044.1>.
- Nguyen, L.T. and Molinari, J. (2015) Simulation of the downshear reformation of a tropical cyclone. *Journal of the Atmospheric Sciences*, 72, 4529–4551. <https://doi.org/10.1175/JAS-D-15-0036.1>.
- Paulson, C.A. and Simpson, J.J. (1977) Irradiance measurements in the upper ocean. *Journal of Physical Oceanography*, 7, 953–956.
- Persing, J., Montgomery, M.T., McWilliams, J.C. and Smith, R.K. (2013) Asymmetric and axisymmetric dynamics of tropical cyclones. *Atmospheric Chemistry and Physics*, 13, 12299–12341. <https://doi.org/10.5194/acp-13-12299-2013>.
- Powell, M., Vickery, P. and Reinhold, T. (2003) Reduced drag coefficient for high wind speeds in tropical cyclones. *Nature* 422, 279–283. <https://doi.org/10.1038/nature01481>.
- Rogers, R. (2010) Convective-scale structure and evolution during a high-resolution simulation of tropical cyclone rapid intensification. *Journal of the Atmospheric Sciences*, 67, 44–70. <https://doi.org/10.1175/2009JAS3122.1>.
- Sandery, P.A., Brassington, G.B., Craig, A. and Pugh, T. (2010) Impacts of ocean-atmosphere coupling on tropical cyclone intensity change and ocean prediction in the Australian region. *Monthly Weather Review*, 138, 2074–2091. <https://doi.org/10.1175/2010MWR3101.1>.
- Van Sang, N., Smith, R.K. and Montgomery, M.T. (2008) Tropical-cyclone intensification and predictability in three dimensions. *Quarterly Journal of the Royal Meteorological Society*, 134, 563–582. <https://doi.org/10.1002/qj.235>.
- Sanger, N.T., Montgomery, M.T., Smith, R.K. and Bell, M.M. (2014) An observational study of tropical cyclone spinup in super typhoon Jangmi (2008) from 24 to 27 September. *Monthly Weather Review*, 142, 3–28. <https://doi.org/10.1175/MWR-D-12-00306.1>.
- Schade, L.R. and Emanuel, K.A. (1999) The ocean's effect on the intensity of tropical cyclones: results from a simple coupled atmosphere-ocean model. *Journal of the Atmospheric Sciences*, 56, 642–651. [https://doi.org/10.1175/1520-0469\(1999\)056<0642:TOSEOT>2.0.CO;2](https://doi.org/10.1175/1520-0469(1999)056<0642:TOSEOT>2.0.CO;2).
- Shchepetkin, A.F. and McWilliams, J.C. (2005) The regional oceanic modeling system (ROMS): a split-explicit, free-surface, topography-following-coordinate oceanic model. *Ocean Modelling*, 9, 347–404. <https://doi.org/10.1016/j.ocemod.2004.08.002>.
- Shchepetkin, A.F. and McWilliams, J.C. (2009) Correction and commentary for “Ocean forecasting in terrain-following coordinates: formulation and skill assessment of the regional ocean modeling system” by Haidvogel et al., *J. Comp. Phys.* 227, pp. 3595–3624. *Journal of Computational Physics*, 228, 8985–9000.
- Shin, H.H. and Hong, S.Y. (2015) Representation of the subgrid-scale turbulent transport in convective boundary layers at gray-zone resolutions. *Monthly Weather Review*, 143, 250–271. <https://doi.org/10.1175/MWR-D-14-00116.1>.
- Simpson, R.H. and Saffir, H. (1974) The hurricane disaster—potential scale. *Weatherwise*, 27, 169–186. <https://doi.org/10.1080/00431672.1974.9931702>.
- Skamarock, W.C. and Coauthors. (2019) *A Description of the Advanced Research WRF Model Version 4*. Boulder, CO, USA: National Center for Atmospheric Research, p. 145.
- Smagorinsky, J. (1963) General circulation experiments with the primitive equations. *Monthly Weather Review*, 91, 99–164. [https://doi.org/10.1175/1520-0493\(1963\)091<0099:GCEWTP>2.3.CO;2](https://doi.org/10.1175/1520-0493(1963)091<0099:GCEWTP>2.3.CO;2).
- Stauffer, D.R. and Seaman, N.L. (1994) Multiscale four-dimensional data assimilation. *Journal of Applied Meteorology*, 33, 416–434. [https://doi.org/10.1175/1520-0450\(1994\)033<0416:MFDDA>2.0.CO;2](https://doi.org/10.1175/1520-0450(1994)033<0416:MFDDA>2.0.CO;2).
- Steranka, J., Rodgers, E.B. and Gentry, R.C. (1986) The relationship between satellite measured convective bursts and tropical cyclone intensification. *Monthly Weather Review*, 114, 1539–1546. [https://doi.org/10.1175/1520-0493\(1986\)114<1539:TRBSMC>2.0.CO;2](https://doi.org/10.1175/1520-0493(1986)114<1539:TRBSMC>2.0.CO;2).
- Tao, C. and Jiang, H. (2015) Distributions of shallow to very deep precipitation-convection in rapidly intensifying tropical cyclones. *Journal of Climate*, 28, 8791–8824. <https://doi.org/10.1175/JCLI-D-14-00448.1>.
- Tao, D. and Zhang, F. (2015) Effects of vertical wind shear on the predictability of tropical cyclones: practical versus intrinsic limit. *Journal of Advances in Modeling Earth Systems*, 7, 1534–1553. <https://doi.org/10.1002/2015MS000474>.
- Tewari, M., and Coauthors, 2004: *Implementation and verification of the unified NOAA land surface model in the WRF model*. 20th Conference on Weather Analysis and Forecasting/16th Conference on Numerical Weather Prediction, pp. 11–15.
- Trabing, B.C. and Bell, M.M. (2020) Understanding error distributions of hurricane intensity forecasts during rapid intensity changes. *Weather and Forecasting*, 35, 2219–2234. <https://doi.org/10.1175/WAF-D-19-0253.1>.
- Vincent, E.M., Lengaigne, M., Vialard, J., Madec, G., Jourdain, N.C. and Masson, S. (2012) Assessing the oceanic control on the amplitude of sea surface cooling induced by tropical cyclones. *Journal*

- of *Geophysical Research: Oceans*, 117(C5), 1–14. <https://doi.org/10.1029/2011JC007705>.
- Wang, B. and Zhou, X. (2008) Climate variation and prediction of rapid intensification in tropical cyclones in the western North Pacific. *Meteorology and Atmospheric Physics*, 99, 1–16. <https://doi.org/10.1007/s00703-006-0238-z>.
- Wang, X. and Jiang, H. (2021) Contrasting behaviors between the rapidly intensifying and slowly intensifying tropical cyclones in the North Atlantic and eastern Pacific basins. *Journal of Climate*, 34, 987–1003. <https://doi.org/10.1175/JCLI-D-19-0908.1>.
- Warner, J.C., Sherwood, C.R., Signell, R.P., Harris, C.K. and Arango, H.G. (2008) Development of a three-dimensional, regional, coupled wave, current, and sediment-transport model. *Computational & Geosciences*, 34, 1284–1306. <https://doi.org/10.1016/j.cageo.2008.02.012>.
- Warner, J.C., Armstrong, B., He, R. and Zambon, J.B. (2010) Development of a coupled ocean–atmosphere–wave–sediment transport (COAWST) modeling system. *Ocean Modelling*, 35, 230–244. <https://doi.org/10.1016/j.ocemod.2010.07.010>.
- Ying, M., Zhang, W., Yu, H., Lu, X., Feng, J., Fan, Y.X., Zhu, Y. and Chen, D. (2014) An overview of the China Meteorological Administration tropical cyclone database. *Journal of Atmospheric and Oceanic Technology*, 31, 287–301. <https://doi.org/10.1175/JTECH-D-12-00119.1>.
- Yu, Y., Gao, H., Shi, J., Guo, X. and Liu, G. (2017) Diurnal forcing induces variations in seasonal temperature and its rectification mechanism in the eastern shelf seas of China. *Journal of Geophysical Research: Oceans*, 122, 9870–9888. <https://doi.org/10.1002/2017JC013473>.
- Yu, Y. and Coauthors. (2020) Importance of diurnal forcing on the summer salinity variability in the East China Sea. *Journal of Physical Oceanography*, 50, 633–653. <https://doi.org/10.1175/JPO-D-19-0200.1>.
- Zeng, Z., Wang, Y. and Wu, C.-C. (2007) Environmental dynamical control of tropical cyclone intensity—an observational study. *Monthly Weather Review*, 135, 38–59. <https://doi.org/10.1175/MWR3278.1>.
- Zhang, D.-L., Liu, Y. and Yau, M.K. (2001) A multiscale numerical study of hurricane Andrew (1992). Part IV: unbalanced flows. *Monthly Weather Review*, 129, 92–107. [https://doi.org/10.1175/1520-0493\(2001\)129<0092:AMNSOH>2.0.CO;2](https://doi.org/10.1175/1520-0493(2001)129<0092:AMNSOH>2.0.CO;2).
- Zhang, F. and Tao, D. (2013) Effects of vertical wind shear on the predictability of tropical cyclones. *Journal of the Atmospheric Sciences*, 70, 975–983. <https://doi.org/10.1175/JAS-D-12-0133.1>.

How to cite this article: Yu, Y., Chen, S.-H., Tseng, Y.-H., Foltz, G.R., Zhang, R.-H. & Gao, H. (2022) Impacts of model resolution and ocean coupling on mean and eddy momentum transfer during the rapid intensification of super-typhoon Muifa (2011). *Quarterly Journal of the Royal Meteorological Society*, 148(749), 3639–3659. Available from: <https://doi.org/10.1002/qj.4379>